THE JOURNAL OF PHYSICAL CHEMISTRY C
A JOURNAL OF THE AMERICAN CHEMICAL SOCIETY

pubs.acs.org/JPCC

Article

Scheelite-Type Wide-Bandgap ABO_4 Compounds (A = Ca, Sr, and Ba; B = Mo and W) as Potential Photocatalysts for Water Treatment

Marta Kowalkińska,* Paweł Głuchowski, Tomasz Swebocki, Tadeusz Ossowski, Adam Ostrowski, Waldemar Bednarski, Jakub Karczewski, and Anna Zielińska-Jurek*

Cite This: https://doi.org/10.1021/acs.jpcc.1c06481

Read Online

ACCESS | Metrics & More | Article Recommendations | Supporting Information

ABSTRACT: In the present study, alkaline earth metal scheelite-type ABO_4 compounds (A = Ca, Sr, and Ba; B = Mo and W) synthesized by a hydrothermal method were systematically studied. The as-obtained photocatalysts were characterized by X-ray diffraction (XRD), scanning electron microscopy (SEM), Brunauer–Emmett–Teller (BET) surface area analysis, UV–vis diffuse reflectance (DR/UV–vis) spectroscopy, photoluminescence, and thermoluminescence (TL) spectroscopy together with charge carrier lifetime measurements, electron paramagnetic resonance (EPR) spectroscopy, and electrochemical impedance spectroscopy (EIS). The photocatalytic activity was studied in the reaction of phenol degradation under simulated solar light. The obtained tungstates and molybdates revealed excellent photocatalytic activity despite the low surface area and wide bandgap typical for insulators. The mechanism of phenol degradation proceeded through hydroquinone and catechol formation in the presence of hydroxyl and superoxide radicals. The presence of electron traps allowed absorption of light with lower energy than resulting from the absorption edge. $BaWO_4$ and $SrWO_4$, with the most extended average carrier lifetime, were the most efficient photocatalysts from the obtained series. In general, molybdates exhibited lower photocatalytic activity toward phenol degradation due to deeper trap states and lower average charge carrier lifetimes than tungstates. Additionally, electrochemical studies demonstrated that molybdates exhibit more insulating behavior than tungstates. The overall results showed that wide-bandgap semiconductors, mainly tungstates, can be applied as earth-abundant photocatalytic materials for the degradation of persistent organic pollutants.

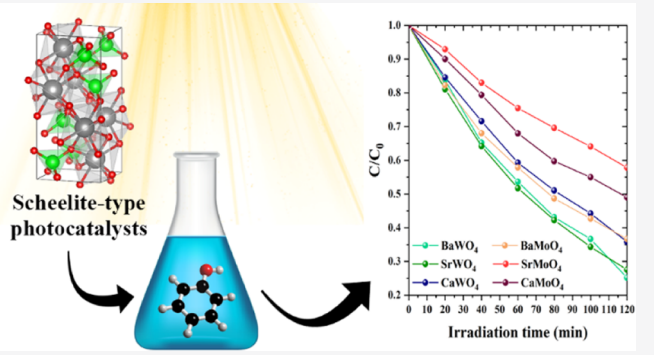

1. INTRODUCTION

The environmental pollution due to increased agricultural, industrial, and domestic activities has led to the global need to develop advanced and more effective water treatment technologies. Heterogeneous photocatalysis belonging to the group of advanced oxidation processes (AOPs) has been demonstrated as a green technology for removing toxic contaminants and energy production. The main advantage is the possibility of light-induced degradation of the broad spectrum of recalcitrant organic pollutants.[1−5] The most frequently studied photocatalysts include oxides, sulfides, selenides, and iodides as single and hybrid compounds.[6] However, the ability to apply heterogeneous photocatalysis in wastewater treatment at a full technological scale requires the application of earth-abundant photocatalytic materials, whose preparation method will not be expensive or sophisticated.

Many inorganic solids from the class of materials with ABO_4 composition occur naturally, including $CaWO_4$ (scheelite) or $CaMoO_4$ (powellite).[7] Scheelite-type compounds with the composition ABO_4, in which A and B cations are different elements with various oxidation states, have been investigated in recent years due to their attractive properties and potential applications as Raman lasers,[8,9] cryogenic scintillation detectors,[10,11] white light-emitting diodes,[12] and a highly suitable host for luminescent materials due to thermal and chemical stability.[12−14] The synthesis of these materials can be cost-effective and simple; the most popular method is a facile co-precipitation.[15] Scheelite-type compounds possess a tetragonal structure characterized by a $I41/a$ space group (no. 88). Each of the B atoms (B = Mo and W) is 4-fold-coordinated, forming the $[BO_4]^{2-}$ tetrahedral configuration, while each divalent metal A^{II} shares corners with eight adjacent oxygen atoms from the $[BO_4]^{2-}$ tetrahedra, composing the AO_8 polyhedra (bisdisphenoid).[16] The scheelite structure, which

Received: July 20, 2021
Revised: October 28, 2021

was visualized using the VESTA program,[17] is presented in Figure 1.

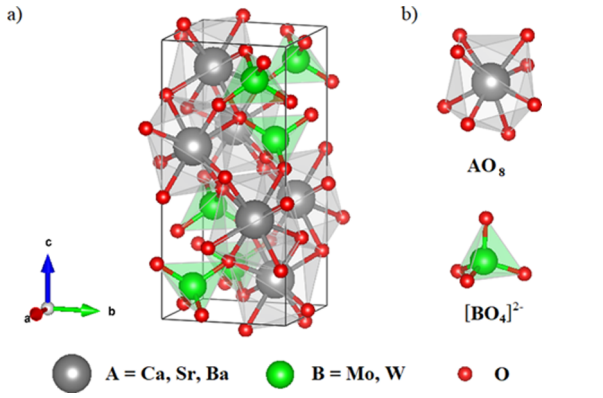

Figure 1. Visualization of the (a) scheelite structure, (b) AO_8, and $[BO_4]^{2-}$ polyhedra.

Since scheelite-type compounds are mainly semiconductors, they are supposed to have photocatalytic properties. Previous sparse studies have focused on the possibility of application ABO_4 compounds in photocatalytic degradation of organic dyes,[18−20] salicylic acid,[21] tetracycline, or hydrogen generation.[22] However, in these reports, for scheelite-type compounds due to their wide bandgaps of about 4−5 eV, only high energy-consuming ultraviolet radiation was applied to study the efficiency of photocatalytic processes. However, the high value of E_g does not have to be an obstacle for the application of scheelite-type materials as photocatalysts because it may increase the valence band maximum to higher energy levels relative to the redox potentials of adsorbed molecules. This rise might contribute to the higher reactivity of electrons in semiconductors.[23] For example, Dong *et al.* demonstrated the O-vacancy defects present in the typical insulator $BaCO_3$, which played dominant roles in the photocatalytic removal of NO.[24] Similar observations were also noticed by Cui *et al.* in $BaSO_4$ with intrinsic Ba vacancy.[25] All of these examples suggest that scheelite-type compounds containing Ba, Sr, or Ca cations might exhibit good photocatalytic performance, despite large values of E_g. The wide-bandgap photocatalysts can be used as a co-catalyst to facilitate the migration of charge carriers from the semiconductor photocatalyst or a locked layer to prevent the recombination of charge carriers.[26]

In this regard, in the present study, the alkaline earth tungstates and molybdates with interesting luminescence and structural properties were studied for the first time as potential alkali earth metal-abundant photocatalytic materials. Alkaline earth metal scheelite-type ABO_4 compounds (A = Ca, Sr, and Ba; B = Mo and W) as examples of wide-bandgap semiconductors were applied for phenol photodegradation. Phenol was selected as a model pollutant since it is photostable and non-volatile, and the mechanism of phenol degradation is well established. Moreover, phenol is produced by chemical, food-processing, or biotechnological industries. Phenol and its derivatives are hardly biodegradable and have a phytotoxic effect on the microorganisms responsible for their biological degradation.[27,28] Also, the current phenol levels and removal of their derivatives from water, which can be achieved using conventional water treatment technologies, are often unsatisfactory. The photocatalytic degradation of phenol in water starts with the formation of a phenoxy radical due to the reaction between phenol molecules and photocatalytically generated hydroxyl radicals ($^{\bullet}OH$). These phenoxy radicals are in resonance with two radical structures in the ortho- and para-positions; thus, di-hydroxylated side products, such as catechol and hydroquinone, are formed. After that, further oxidation of phenol derivatives occurs, and finally, the photocatalytic process leads to the opening of the benzene ring and the formation of shorter aliphatic compounds, which can be easily mineralized to carbon(IV) dioxide.[29,30] However, phenol photocatalytic degradation is still challenging because it is dependent on the efficiency of the generation of reactive oxygen species (ROS), especially $^{\bullet}OH$ and $^{\bullet}O_2^-$ radicals. Aslam *et al.* have reported that superoxide radicals were the major contributors in phenol degradation because only the $^{\bullet}O_2^-$ radicals can open the phenyl ring and contribute to the loss of aromaticity. These observations were noticed for disc-shaped WO_3 photocatalysts.[31]

The main aim of the present work was the demonstration of alkaline earth metal tungstates and molybdates as potential photocatalysts in a broad sense, including also crucial differences between tungstates and molybdates. The ABO_4 compounds were studied for the first time as potential alkali earth metal-abundant materials for UV−vis light-induced phenol photocatalytic degradation. Furthermore, the effects of morphology, their electrochemical and optical properties, and their influence on the mechanism of phenol degradation were also studied in detail.

2. METHODS

2.1. Fabrication of Metal Tungstates and Molybdates. Alkaline earth metal tungstates and molybdates, namely, $CaWO_4$, $SrWO_4$, $BaWO_4$, $CaMoO_4$, $SrMoO_4$, and $BaMoO_4$, were synthesized by a hydrothermal method without using any surfactant or stabilizing agent. Calcium chloride ($CaCl_2$), strontium chloride hexahydrate ($SrCl_2{\cdot}6H_2O$), barium nitrate ($Ba(NO_3)_2$), sodium tungstate dihydrate ($Na_2WO_4{\cdot}2H_2O$), and sodium molybdate dihydrate ($Na_2MoO_4{\cdot}2H_2O$) were used as received from Sigma-Aldrich without any purification. In a typical synthesis of scheelite-type compounds, a stoichiometric amount of alkali metal salts and $Na_2WO_4{\cdot}2H_2O$ (metal tungstates) or $Na_2MoO_4{\cdot}2H_2O$ (metal molybdates) were dissolved in 50 cm^3 distilled water separately. The solution containing sodium molybdates or tungstates was placed inside a 200 cm^3 Teflon-lined reactor, and the second solution was added dropwise to the reactor. The obtained mixtures were stirred for 30 min to form stable suspensions using a Teflon-coated magnetic stirrer bar. After that, the reactor was transferred into a stainless steel autoclave immediately and was heated at 160 °C for 6 h in an oven and then cooled down to room temperature. The obtained products were separated through centrifugation and were washed thoroughly with deionized water to remove the residual contamination. After drying at 80 °C to dry mass, the white powders were obtained.

2.2. Material Characterization. The structure and phase composition of the obtained compounds were investigated by powder X-ray diffraction (XRD). XRD patterns were recorded on the Rigaku MiniFlex 600 X-ray diffractometer with Cu Kα radiation (λ = 1.5405 Å) in the 10−80° range (step 1°/min). Rietveld refinements of the diffraction data were performed using the X'Pert HighScorePlus software package (PANalytical, 2006) with data fitting based on the pseudo-Voigt profile

https://doi.org/10.1021/acs.jpcc.1c06481
J. Phys. Chem. C XXXX, XXX, XXX−XXX

function. The specimen displacement, lattice parameters, polynomial coefficients for the background function, profile parameters, and Gaussian and Lorentzian profile coefficients were refined.

The alkaline earth tungstates and molybdate morphologies were characterized by scanning electron microscopy (SEM) with a field emission gun, model FEI Quanta FEG 250. In addition, the Micromeritics Gemini V instrument was used to determine the porous structure parameters of the scheelite-type compounds and adsorption isotherms, including Brunauer–Emmett–Teller (BET) surface area and pore volume, using low-temperature nitrogen sorption. Before measurement, the analyzed materials were degassed at 200 °C for 2 h. The surface area was determined by the multipoint BET method in the p/p_0 range from 0.05 to 0.30. The total pore volumes were estimated from the adsorbed amount of nitrogen at $p/p_0 = 0.995$. The average pore diameters were calculated from adsorption isotherms according to the procedure described in Soltanali and Darian.[32] By using the Barrett–Joyner–Halenda (BJH) method, pore size distributions were derived from the branches of the adsorption isotherms.

2.3. Optical Properties. The UV–visible diffuse reflectance spectra (DRS/UV–vis) were measured on a Thermo Fisher Scientific Evolution 220 spectrophotometer using $BaSO_4$ as a reflectance standard. Based on the obtained data, the bandgap energy calculations were performed using Tauc's method.[33] The excitation and luminescence spectra were recorded using an FLS980 fluorescence spectrophotometer from Edinburg Instruments equipped with a 450 W xenon lamp as an excitation source and a Hamamatsu 928 PMT detector. Measured spectra were corrected for the sensitivity and wavelength of the experimental setup. The slit width was 2 μm (excitation spectra) or 0.3 μm (emission spectra). The same equipment was used for decay measurements, and the lamp was changed to a 150 W pulse xenon lamp. All spectra were recorded at room temperature. Based on these measurements, the carrier lifetime of photocatalysts was calculated. The best luminescence decay curve fits of the data were noticed from a poly-phase exponential decay function with time constant parameters (eq 1)

$$I(t) = \sum_{i=1}^{n} \alpha_i \cdot \exp\left(-\frac{t}{\tau_i}\right) + y_0 \tag{1}$$

where $I(t)$ is the intensity, α_i is the pre-exponential scaling factor, $\langle\tau\rangle$ is the lifetime of the ith exponential component, and y_0 is a constant. The average lifetime $\langle\tau\rangle$ is given by eq 2

$$\langle\tau\rangle = \frac{\sum_{i=1}^{n} \alpha_i \tau_i^2}{\sum_{i=2}^{n} \alpha_i \tau_i} \tag{2}$$

The errors associated with the carrier lifetime evaluations consider only the uncertainty in decay curve fitting.[34,35]

The thermoluminescence (TL) glow curves were collected from room temperature up to 300 °C with a heating rate of 5 K/s after 5 min of X-ray irradiation. A Varian VF-50J/S RTG tube with a tungsten core and copper case as an X-ray radiation source was used as an irradiation source. The voltage and amperage for the X-ray source were 35 kV and 0.7 mA, respectively. The signal was collected with an R13456 PMT (Hamamatsu Photonics) monitoring the global emission from the whole spectral response (from 185 to 980 nm) with an integration (channel) time of 0.1 s without a filter. The energy of the traps was calculated according to the general-order expression describing intensity I as a function of temperature T (eq 3)[36,37]

$$I(T) = sn_0 \cdot \exp\left(\frac{E}{k_B T}\right) \cdot \left[\frac{(l-1)s}{\beta} \cdot \int_{T_0}^{T} \exp\left(-\frac{E}{k_B T}\right) dT + 1\right]^{-l(l-1)} \tag{3}$$

where n_0 is the trap concentration at $t = 0$, k_B is Boltzmann's constant, and β is the heating rate. The kinetics order l was determined from the peak asymmetry defined as the thermal activation energy E. The parameter E is associated with the trap depth, assuming no re-trapping. The frequency factor s was obtained by taking the derivative of eq 3 with respect to T and setting it to zero at the peak temperature.

2.4. Electrode Surface Preparation, Electrochemical Measurements, and EPR Studies. Preparation of the electrode substrates modified with ABO_4 photocatalysts, suitable for electrochemical measurements, was performed in three stages: pretreatment, deposition of the sample, and surface blockage. Each sample was deposited onto FTO electrodes (7 Ω/sq) (Sigma Aldrich), 35 × 15 mm by size, by drop-casting a suspension of samples (V_{drop} = 0.005 cm^3). The suspension was prepared by mixing water/isopropanol solution (v/v: 3/1) with *ca.* 0.06 mol of the given sample. The suspension were then sonicated for a couple of seconds and drop-cast onto the electrode, followed by drying to evaporate the solvent completely. The surface blockage was carried out by spin-coating 0.1 cm^3 of Nafion (Sigma-Aldrich) onto the FTO surface (200 rpm). After this step, the electrodes were placed in the electrochemical cell for further experiments.

Electrochemical measurements were performed in a glass cell with a built-in cylindrical glassy carbon (GC) auxiliary electrode. A silver chloride (3 M KCl) electrode was used as a reference. A 0.25 M Na_2SO_4 was used as a supporting electrolyte, and a 2.5 mM solution of potassium hexacyanoferrate(II/III) $[Fe(CN)_6]^{3-/4-}$ was chosen as a redox probe. An Autolab Multi M204 potentiostat/galvanostat with the FRA32 module (Metrohm) was used for electrochemical measurements, and a built-in software, Nova 2.1.4., was used for EIS spectra fitting.

In the photochemical EPR experiments, the samples were prepared as an aqueous suspension of $BaWO_4$ or $SrWO_4$ (concentration 0.4 g cm^{-3}) in the presence of α-phenyl-*N*-*tert*-butylnitrone (PBN) spin trap (concentration 60 mmol dm^{-3}) at room temperature. Approximately 0.017 cm^3 mixture of PBN and $BaWO_4$ or $SrWO_4$ aqueous suspension was placed into a thin-walled quartz tube with 0.8 mm ID and put in an EPR cavity. LG UV LED (3 W, λ_{max} = 365 nm) was used as an irradiation source. During photochemical EPR experiments, the samples were irradiated directly in the EPR resonator with a light power of about 70 mW/cm^2. EPR measurements were performed both for samples obtained under aerobic and hypoxic conditions. For studies under aerobic or hypoxic conditions, air or N_2 was passed over the sample at a rate of a few dm^3 h^{-1}.

2.5. Determination of Photocatalytic Activity. The photocatalytic activity of the obtained samples was tested in a phenol degradation reaction performed in the black box. All mentioned chemicals were used as delivered by the provider

https://doi.org/10.1021/acs.jpcc.1c06481
J. Phys. Chem. C XXXX, XXX, XXX–XXX

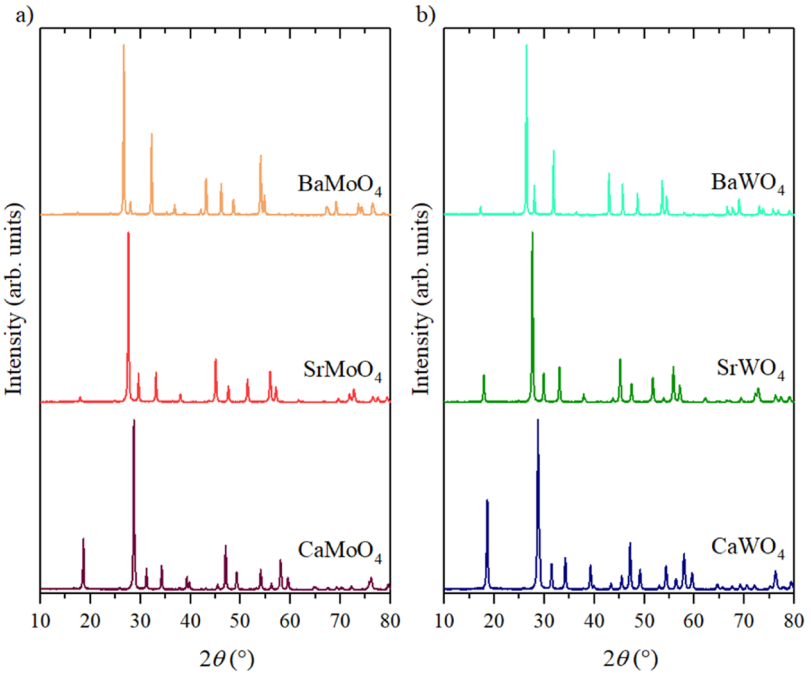

Figure 2. XRD patterns of obtained (a) molybdates and (b) tungstates.

Table 1. Structural Parameters of the Obtained Samples Using Rietveld Analysis

		lattice parameters			cation−oxygen distance		Rietveld refinement[a]		
compound	crystallite size estimation (nm)	a, b (Å)	c (Å)	V (Å^3)	A−O (Å)	B−O (Å)	R_{exp}(%)	R_{wp} (%)	χ^2
$CaMoO_4$	50	5.225	11.432	312.18	2.448 2.477	1.749	10.76	13.51	1.58
$SrMoO_4$	43	5.395	12.023	350.01	2.619 2.626	1.735	9.39	11.99	1.63
$BaMoO_4$	47	5.582	12.823	399.50	2.800 2.808	1.697	9.43	12.80	1.35
$CaWO_4$	31	5.240	11.368	312.10	2.358 2.514	1.890	10.20	12.70	1.55
$SrWO_4$	41	5.415	11.945	350.21	2.529 2.533	1.862	9.16	11.82	1.67
$BaWO_4$	75	5.612	12.721	401.70	2.704 2.753	1.825	9.73	12.52	1.30

[a]The uncertainty of structural parameters, including lattice constants and bond lengths, is strictly correlated with a Rietveld refinement quality. The insight into how well the model fits the experimental data is determined by expected profile residual (R_{exp}), weighted profile residual (R_{wp}), and goodness of fit (χ^2).

and were used without any purification. In a typical experiment of phenol photocatalytic degradation, 25 cm^3 of 0.21 mmol dm^{-3} phenol solution and 50 mg of the photocatalyst were put into a quartz reactor under magnetic stirring. A xenon lamp (model 6271H, Oriel, USA) was used as a simulated solar light source with a narrow range of UV light.[38] The UV spectrum flux intensity at the reactor border was set as 45 mW cm^{-2}. A constant air flow of 5 dm^3 h^{-1} was introduced during the reaction through suspension, which was thermostated to 20 °C. Before irradiation, the whole system was kept in the dark for 30 min to achieve the adsorption−desorption equilibrium. After that, the process was initiated by turning on the Xe lamp. The samples were collected at −30, 0, 20, 40, 60, 80, 100, and 120 min of the process, where 0 is the point of light introduction. The degradation efficiency was monitored using a high-performance liquid chromatography system (HPLC, model Shimadzu LC-6A), combined with a photodiode array detector (SPD-M20A) and a C18 column (Phenomenex Gemini 5 μm; 150 × 4.6 mm) working at 45 °C. During HPLC measurements, the mobile phase composed of (v/v) 70% acetonitrile, 29.5% water, and 0.5% orthophosphoric acid (85% w/w solution) was used at a flow rate of 0.3 cm^3 min^{-1}. Quantitative analysis of all the observed species was performed using standard compounds from Sigma-Aldrich using the external calibration method. An HPLC-grade acetonitrile and orthophosphoric acid solution was provided by Merck. Charge carrier scavengers, such as ammonium oxalate, silver nitrate, isopropyl alcohol, and benzoquinone, were provided by Sigma-Aldrich. Simultaneously, the total organic carbon (TOC) concentration after each process was monitored using the Shimadzu TOC-L analyzer.

https://doi.org/10.1021/acs.jpcc.1c06481
J. Phys. Chem. C XXXX, XXX, XXX−XXX

3. RESULTS AND DISCUSSION

3.1. Structural and Morphological Analysis. To confirm the presence of single-phase metal tungstates and molybdates, XRD was performed, and the obtained patterns are presented in Figure 2. According to Rietveld analysis and CIF files, single-phase compounds with high crystallinity were successfully obtained. The refinement results revealed that all compounds crystallized in the tetragonal scheelite structure with the space group $I41/a$ and a good agreement between the recorded and calculated patterns were observed. The refined structural parameters of scheelite compounds are presented in Table 1. The lattice parameters (a and c) and the unit cell volume rise with the increasing ionic radii of alkaline earth ions (Ca^{2+} = 0.112 nm, Sr^{2+} = 0.125 nm, and Ba^{2+} = 0.142 nm) due to the change in the charge density of AO_8 together with the rise of metal's ionic radii.[16]

Additionally, the relative intensity of some peaks was changed in the same relation. For example, the signal at 20° 2θ originating from the (101) $CaMoO_4$ plane was lowered when the Ca atom was replaced by a heavier one and almost completely vanished in $BaMoO_4$. The average crystallite size was estimated from the (112) peaks at 30° 2θ using Scherrer's equation. The greatest crystallite size was noticed for $BaWO_4$, in which both the heaviest cation and transition metal were present.

The morphologies of alkali earth metal molybdates and tungstates were further studied by scanning electron microscopy analysis. Size distributions of particles or microcrystals are presented in Figure S1 in the Supporting Information. Figure 3a shows the uniform $CaWO_4$ microspheres with an average size of *ca.* 7 μm. These spheres consist of agglomerated nanoparticles with an average size of 79 ± 14 nm (Figure 3b). A similar morphology was observed for the $CaMoO_4$ (Figure 3c,d), $SrWO_4$ (Figure 4a,b), and $SrMoO_4$ (Figure 4c,d) samples, but in comparison with $CaWO_4$, their aggregates were more deformed. Additionally, nanoparticles present in $SrMoO_4$ microspheres were polyhedral, and the exposed crystal facets of nanocrystals can be easily observed. In the case of $BaWO_4$ (Figure 5a) and $BaMoO_4$ (Figure 5b) samples, polyhedra-shaped microcrystals presenting a polydisperse nature were observed. Similar morphologies were noticed by Cavalcante *et al.*[39] and Oliveira *et al.*,[40] suggesting enhanced crystal growth when heavy cations such as barium are introduced to the system. Although the nucleation rate of barium-based materials is slower than for strontium and calcium ones, the crystal growth is the fastest with Ba^{2+}. This effect explains the formation of microcrystals only for $BaMoO_4$ and $BaWO_4$.

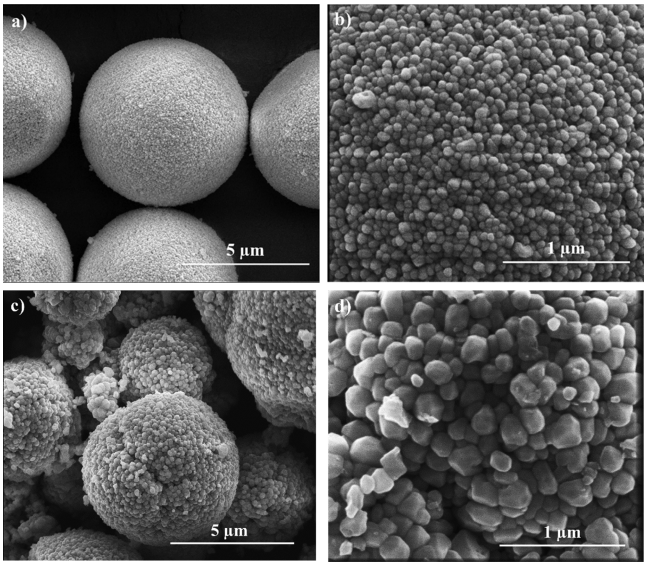

Figure 3. SEM images of $CaWO_4$ (a,b) and $CaMoO_4$ (c,d) microspheres and nanoparticles, respectively.

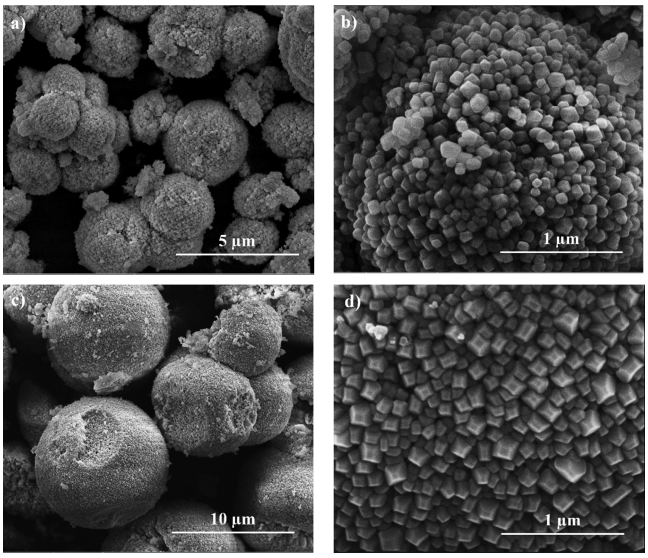

Figure 4. SEM images of $SrWO_4$ (a,b) and $SrMoO_4$ (c,d) microspheres and nanoparticles, respectively.

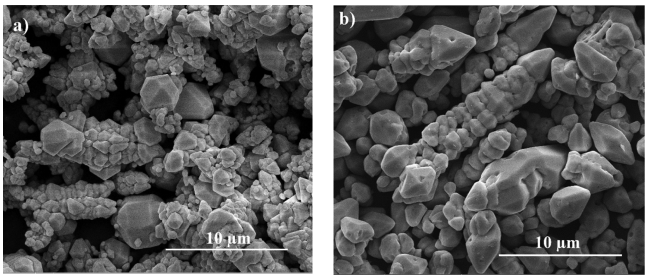

Figure 5. SEM images of $BaWO_4$ (a) and $BaMoO_4$ (b) microcrystals.

The data from electron microscopy were completed by surface area and pore analysis using the BET and BJH methods, as presented in Table 2. More detailed information, including adsorption isotherms and pore size distribution, are presented in Figure S2 in the Supporting Information. All samples were characterized by low surface area. Calcium and strontium compounds, which created the microspheres consisting of agglomerated nanoparticles, had surface areas ranging from 4 to 10 $m^2\ g^{-1}$, while $BaWO_4$ and $BaMoO_4$ possessed a reduced surface area of about 0.4−1 $m^2\ g^{-1}$. These results can be explained as the beginning of the aggregation process and the formation of microcrystals with smooth facets, as observed under SEM images. In the previous reports, the morphology of barium compounds was studied for $BaWO_4$ crystals with {1 1 2}, {0 0 1}, and {1 0 0} as predominantly exposed facets, in which the {1 1 2} facet is commonly the most exposed. However, edge-truncated octahedra can be noticed due to the destabilization of the {1 1 2} surface.[41] The preferential growth was also observed for $BaMoO_4$ crystals,

https://doi.org/10.1021/acs.jpcc.1c06481
J. Phys. Chem. C XXXX, XXX, XXX−XXX

Table 2. Specific Surface Area and Morphology Summation of the Obtained Samples

Sample	surface area (m^2g^{-1})[a]	pore volume (cm^3g^{-1})[a]	mean agglomerate diameter (μm)	mean nanoparticle size (nm)
$CaMoO_4$	3.88 ± 0.17	0.0264 ± 0.0012	5.22 ± 1.18	195 ± 37
$SrMoO_4$	4.21 ± 0.04	0.0386 ± 0.0004	8.62 ± 1.81	141 ± 30
$BaMoO_4$	0.42 ± 0.20	0.0003 ± 0.0001	1.55 ± 0.56	-
$CaWO_4$	10.15 ± 0.29	0.0781 ± 0.0023	6.96 ± 0.94	79 ± 14
$SrWO_4$	6.98 ± 0.13	0.0537 ± 0.0011	2.39 ± 0.67	107 ± 22
$BaWO_4$	1.03 ± 0.14	0.0043 ± 0.0006	1.08 ± 0.70	-

[a]An average of three measurements ± the standard error.

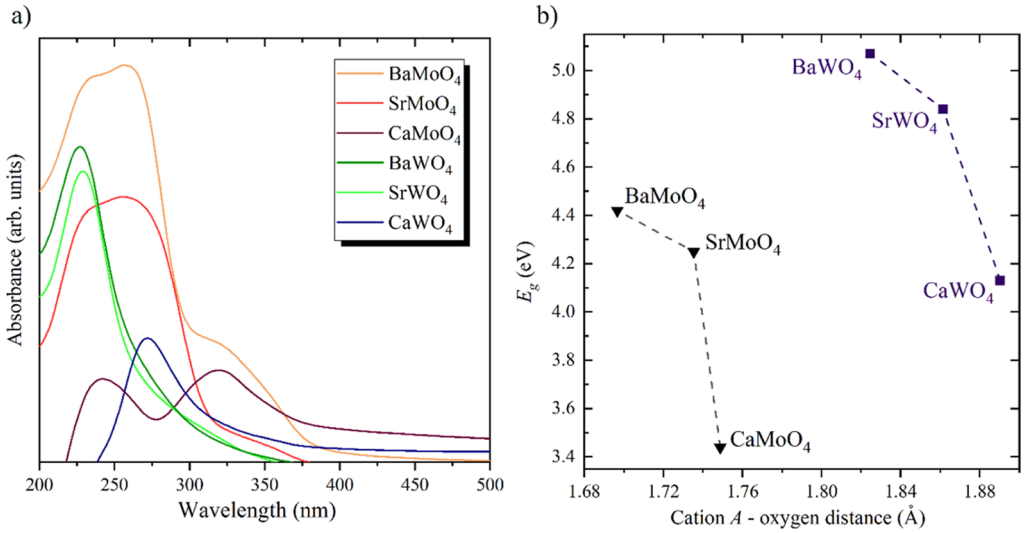

Figure 6. (a) DR/UV−vis spectra of the obtained tungstates and molybdates and (b) relation between the bandgap and the cation−oxygen distance of the obtained samples.

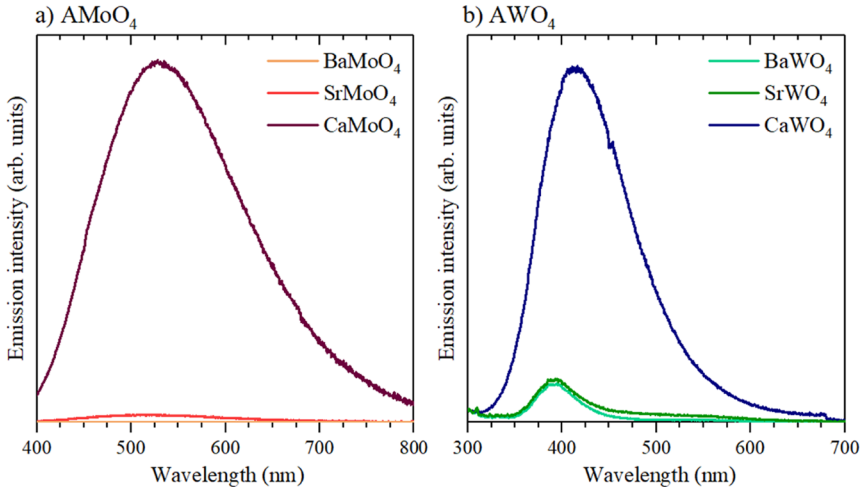

Figure 7. Emission spectra of alkali earth metals: (a) molybdates (λ_{exc} = 260 nm for $BaMoO_4$, λ_{exc} = 265 nm for $SrMoO_4$, and λ_{exc} = 261 nm for $CaMoO_4$) and (b) tungstates (λ_{exc} = 250 nm).

which occur along with the [0 0 1] direction of the micro-octahedrons.[39−41]

3.2. Absorption and Emission Spectroscopy Analysis.

The DR/UV−vis spectra of the obtained ABO_4 photocatalysts are presented in Figure 6a. All the obtained materials absorb light in the UV range, which is typical for wide-bandgap compounds. Therefore, the absorption of solar light irradiation can be limited because only 3−5% of the solar spectrum is ultraviolet light.[42,43] According to the recorded spectra, strontium and barium compounds possess the highest absorbance in the series; however, the absorption behavior is different for tungstates and molybdates. The spectra bands for AWO_4 materials are narrow, and probably single excitation states are observed. In contrast, the bands of $AMoO_4$ compounds are broader, with more overlapping excitation states.

After converting spectra to the Kubelka−Munk functions, the bandgaps of scheelite-type compounds were calculated. The transformations of these functions are presented in the Supporting Information (Figure S3). All photocatalysts are

https://doi.org/10.1021/acs.jpcc.1c06481
J. Phys. Chem. C XXXX, XXX, XXX−XXX

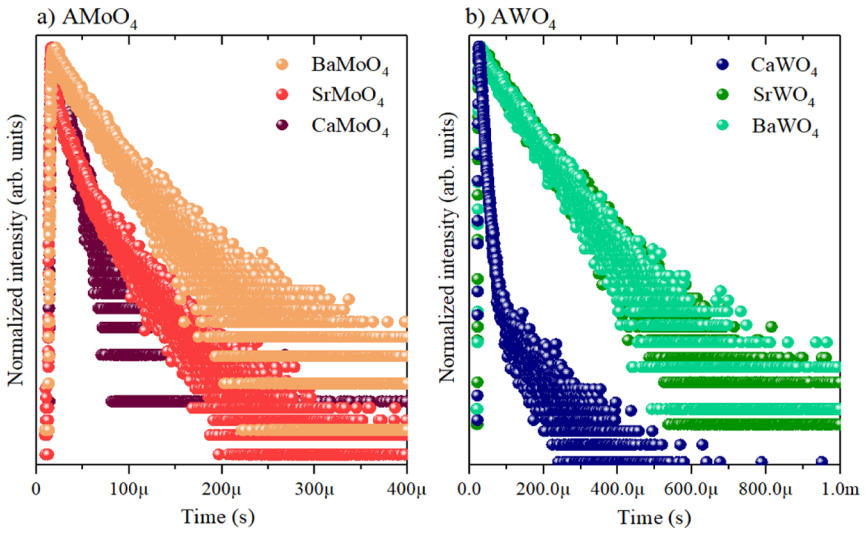

Figure 8. Luminescence decay curve of (a) molybdates (λ_{exc} = 260 nm for $BaMoO_4$, λ_{exc} = 265 nm for $SrMoO_4$, and λ_{exc} = 261 nm for $CaMoO_4$) and (b) tungstates (λ_{exc} = 250 nm).

Table 3. Carrier Lifetimes and Energy Traps for Scheelite-Type Photocatalysts

sample	τ_1 (μs)	τ_2 (μs)	$\langle\tau\rangle$ (μs)	trap energy (eV)
$CaMoO_4$	20.11 ± 2.03	10.89 ± 1.26	17.08 ± 3.71	0.71 ± 0.02
				0.89 ± 0.04
$SrMoO_4$	35.53 ± 0.13	4.17 ± 0.03	8.61 ± 0.10	0.70 ± 0.01
$BaMoO_4$	61.62 ± 2.53	29.98 ± 1.85	50.76 ± 5.22	0.74 ± 0.02
$CaWO_4$	129.61 ± 7.39	10.16 ± 0.03	12.38 ± 0.75	0.65 ± 0.01
				0.87 ± 0.03
$SrWO_4$	110.12 ± 0.35	-	110.12 ± 0.35	0.63 ± 0.01
$BaWO_4$	110.25 ± 0.29	-	110.25 ± 0.29	0.70 ± 0.02

wide-bandgap semiconductors close to the range typical for insulators.[24,44,45] Remarkably for *A* cations, the cation−oxygen distance decreases with the increase of the *A* ionic radius (see in Table 1 and Figure 6b). The reduction of the size of $[BO_4]^{2-}$ tetrahedra with simultaneous changes in AO_8 polyhedra (bisdisphenoid) led to the structural disorder and, in consequence, changed the crystal fields of each cation. The reduced strength of the coordinative bond from O atoms at larger distances led to lower crystal-field splitting. Therefore, it can be observed that the energy gap rises with a decrease of the cation *A*−oxygen distance (an increase of the *A* ionic radius). The same situation occurs if we take into account the cation *B* radii. The larger ion deforms the $[BO_4]^{2-}$ tetrahedra and may lead to a decrease of cation−oxygen distance and, in consequence, increasing the energy gap. This contributes to changes in the absorption properties of the scheelite-type compounds.

The emission spectra of the obtained scheelite-type photocatalysts are presented in Figure 7, while the excitation results are presented in Figure S4 in the Supporting Information. Among the series, the most intense photoluminescence was observed for calcium compounds. These bands, located at about 527 nm ($CaMoO_4$) or 413 nm ($CaWO_4$), were attributed to the intrinsic luminescence of the host lattice.[46,47] It is worth mentioning that the blue emission from $CaWO_4$ and green from $CaMoO_4$ were visible with the naked eye under UV light excitation. While comparing the emission spectra of molybdates (Figure 7a) with those of tungstates (Figure 7b), a blue shift can be seen, especially for $SrWO_4$ and $BaWO_4$. According to Puma and Yue,[48] the degradation rates can be significantly enhanced by shifting the irradiation toward a lower wavelength (higher energy). Therefore, although the emission intensity for $BaWO_4$ and $SrWO_4$ is lower (compared with $CaWO_4$ and $CaMoO_4$), their photoactivity can be higher due to the higher emission energy.

Generally, the photoluminescence emission is strongly connected with radiative recombination processes because they result from optically excited semiconductors. The excitonic photoluminescence signal can origin from surface oxygen vacancies or defects of semiconductors. The lattice distortions may positively impact the photocatalytic performance because they can easily bind electrons to form excitons in the sub-band.[49,50] As the result of the defect binding of the photoinduced electrons, the photoluminescence signal can easily occur. In that case, the stronger the emission signal, the higher the photocatalytic activity, so oxygen vacancies and lattice distortions might favor photocatalytic reactions.[50] On the contrary, lattice distortions can also act as recombination centers that influence the lower photocatalytic performance compared to defect-free samples, as was shown by Liqiang *et al.*[51] Thus, the relation between structural defects and photocatalytic activity is challenging to determine based only on the photoluminescence signals.

In this regard, the optical properties of scheelite-type photocatalysts were completed by decay measurements. The luminescence decay curves and carrier lifetimes calculated from curve fits are presented in Figure 8 and Table 3, respectively. All materials in this series possess an average carrier lifetime in the range *ca.* 9−110 μs. In the $AMoO_4$ series, barium molybdate has the most extended carrier lifetime, whereas, in

https://doi.org/10.1021/acs.jpcc.1c06481
J. Phys. Chem. C XXXX, XXX, XXX−XXX

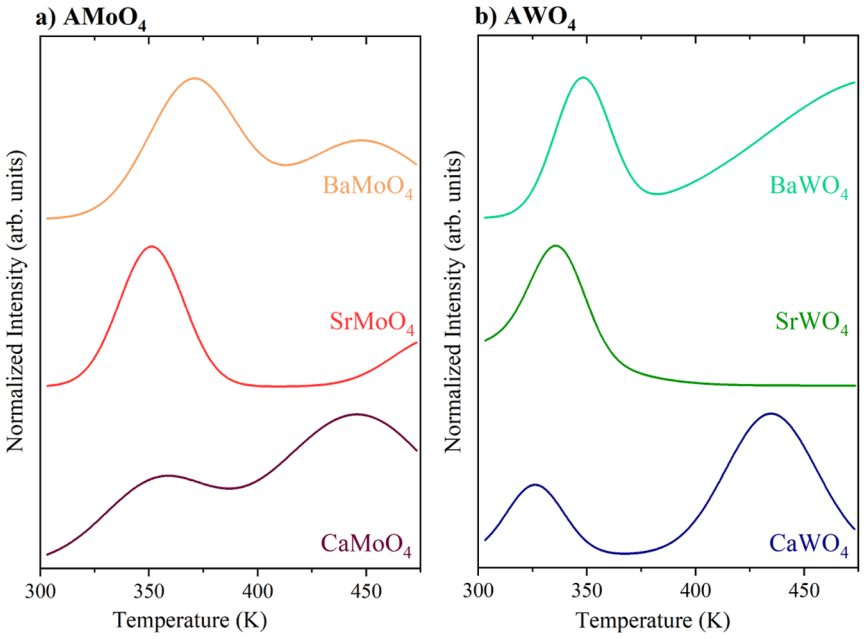

Figure 9. Thermoluminescence glow curves of alkali earth metals: (a) molybdates and (b) tungstates. The measurement was performed after 5 min of X-ray irradiation.

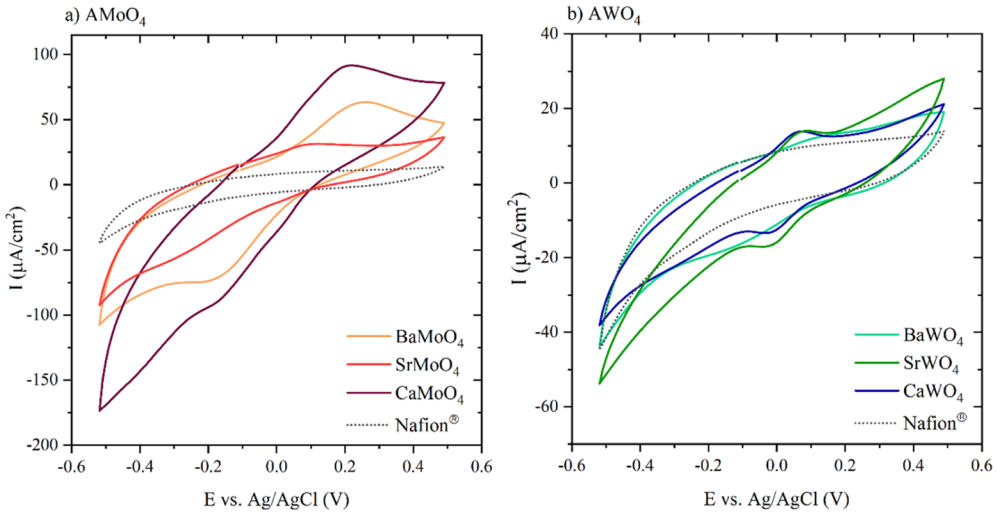

Figure 10. Cyclic voltammograms of (a) $AMoO_4$ and (b) AWO_4 (A = Ba, Ca, and Sr) recorded in the degassed 0.25 M Na_2SO_4 and 2.5 mM $[Fe(CN)_6]^{3-/4-}$ system.

the AWO_4 ones, both strontium and barium tungstates were characterized by the highest $\langle\tau\rangle$ value (110 μs). In general, the carrier lifetime of tungstates was more prolonged than that of molybdates, although the average lifetime for $CaWO_4$ was lower than for $CaMoO_4$. However, the τ_1 parameter for $CaWO_4$ was much higher than for other AWO_4 compounds, suggesting the presence of charge carrier traps. Several attempts at fitting the luminescence decay curves by a single exponential function have been made; however, these calculations were finished successfully only for $SrWO_4$ and $BaWO_4$. The remaining samples required poly-phase exponential decay models, which further suggest that these materials have structural defects in the lattice or the presence of recombination and trapping centers.[51,52] Optical measurements were further followed by electrochemical studies to complete photocatalyst characterization. However, it can be assumed that although the light absorption is limited, the photon amount is sufficient to create photogenerated charge carriers, which are necessary for initiating the photocatalytic reaction.

To confirm the presence of trapping centers in the obtained scheelite-type compounds, thermoluminescence (TL) spectroscopy was performed. Thermoluminescence is a phenomenon that refers to the light emission as a result of heating from an insulator or a wide-bandgap semiconductor that has already been irradiated by a radiation source. High temperatures cause emptying the filled trapping centers obtained from electrons, which then move toward the delocalized bands and finally undergo radiative recombination. The TL parameters of the thermal activation energy are associated with a trap depth.[53] The TL glow curves are presented in Figure 9. A distinct glow in Figure 9a was observed at ~371 and ~352 K for $BaMoO_4$ and $SrMoO_4$, respectively. A similar observation was noticed from Figure 9b for $BaWO_4$ (~348 K) and $SrWO_4$ (~336 K). It

https://doi.org/10.1021/acs.jpcc.1c06481
J. Phys. Chem. C XXXX, XXX, XXX−XXX

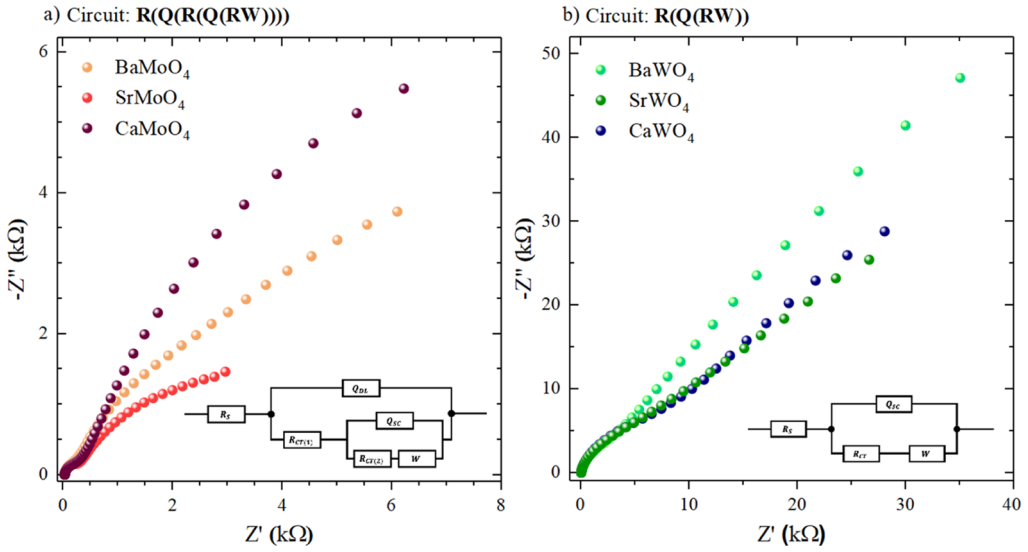

Figure 11. EIS spectra of (a) $AMoO_4$s and (b) AWO_4s (A = Ba, Ca, and Sr) recorded in the degassed 0.25 M Na_2SO_4 and 2.5 mM $[Fe(CN)_6]^{3-/4-}$ system.

is worth highlighting that the calcium compounds can be characterized by two glow peaks (~355 and ~446 K for $CaMoO_4$ and ~327 and ~435 K for $CaWO_4$), which suggest the presence of more than one trapping center.

Considering that the traps are located below the conduction band, it can be supposed that these compounds also absorb light with lower energy than determined by the absorption edge. Therefore, these materials are supposed to be applied as solar-driven photocatalysts. Moreover, the distribution and energy of traps affect photocatalytic efficiency. According to Kong *et al.*, the photocatalytic efficiencies increased with the increasing ratio of the amount of surface to total defects.[54] It was also shown that shallow traps (up to 0.7 eV) have higher electron-transfer efficiency from the defects to the species adsorbed on the surface.[55] The TL studies indicated a significant role of the type of cations *A* and *B* in the creation of electron traps in the scheelite structure, which, consequently, greatly impacts the photocatalytic process. The simple calculation of the energy of the traps (see Table 3) showed that molybdates have deeper traps and therefore should have lower photocatalytic efficiency compared to tungstates. It can also be seen that the scheelite with the smaller *A* cation are characterized by shallower traps, so more electrons can react with molecules such as phenol or water.

3.3. Electrochemical Studies. The profile of the as-synthesized photocatalysts was complemented by electrochemical measurements. First, cyclic voltammograms (CV) were recorded, as presented in Figure 10. By using a negatively charged inorganic probe ($[Fe(CN)_6]^{3-/4-}$), the behavior of the scheelite-type structures incorporated into the Nafion electrode surface was studied. As $[Fe(CN)_6]^{3-/4-}$ is a quasi-reversible probe, both the oxidation and reduction of Fe(II) and Fe(III) form of the probe on a bare, non-modified electrode should be observed. These processes are usually represented on voltammograms by current peaks. By studying the changes in peak height and position, different phenomena regarding the electron transfer can be discussed. The introduction of the Nafion film to the surface of the FTO electrode resulted in complete blockage of the electrode surface as we did not observe the reduction or oxidation process of $[Fe(CN)_6]^{3-/4-}$. This phenomenon can be explained by the nature of Nafion, which is rich in negatively charged SO_3- groups. These groups prevent charge transfer from $[Fe(CN)_6]^{3-/4-}$ due to the electrostatic repulsion of the redox probe.[56]

Meanwhile, implementing scheelite-type compounds into the conductive layer structure resulted in an appearance of slight $[Fe(CN)_6]^{3-/4-}$ peaks and an increase of capacitive currents of the electrode. Molybdates exhibited a much more significant rise in peak currents, with the anodic peak better shaped than the cathodic peak. It is worth mentioning that the difference of redox potential (ΔE) after modification of the surface is equal to *ca.* 370−390 mV. The unequal current response for the redox process together with high values of ΔE indicates the complex mechanism of charge transfer through the layer. We can observe the dependence on the divalent cation for the shape of CV voltammograms and measured currents.

On the other hand, tungstates demonstrated different electrochemical behaviors than molybdates. The recorded voltammograms seem to be less dependent on the cation present in the AWO_4 photocatalyst. Again, the $[Fe(CN)_6]^{3-/4-}$ peaks became visible but with much lower values of the faradaic currents of the probe. The electrochemical process seems to be reversible due to the difference in the reduction and oxidation voltage values of around ΔE *ca.* 82−90 mV. The comparison of the values of the oxidation and reduction current $|I_{pa}/I_{pk}| \approx 1$ confirms the reversibility of the $[Fe(CN)_6]^{3-/4-}$ process. Comparing the results for both groups, the barium and calcium compounds exhibited significantly better electrochemical features than strontium, which impeded the redox process on the electrode.

However, due to the chemical nature of the system and equivocal current changes, electron impedance spectroscopy (EIS) measurements were performed in order to explain the observed phenomenon. The Nyquist plot of EIS spectra of alkali earth metal tungstates and molybdates is presented in Figure 11. Few circuits were tested for data fitting, including R(Q(RW)), R(QR)(QR), and R(Q(R(Q(RW)))), with the last one fitting the best for all the $AMoO_4$ spectra and R(Q(RW)) for AWO_4. The recorded spectra differed in shape—two semi-circles were visible for molybdates, while for

https://doi.org/10.1021/acs.jpcc.1c06481
J. Phys. Chem. C XXXX, XXX, XXX−XXX

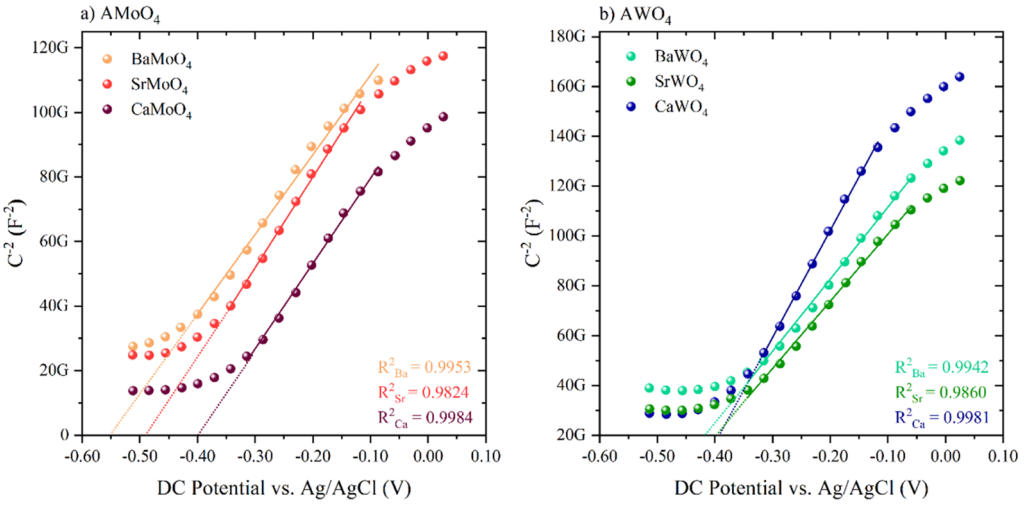

Figure 12. Mott–Schottky diagrams of (a) $AMoO_4$s and (b) AWO_4s (A = Ba, Ca, and Sr).

tungstates, no curvature of mid- to low-frequency impedance plot was observed. The shape of the $AMoO_4$ spectra indicated the possible presence of at least two charge-transfer resistances—one for the obtained material and the other one for FTO itself (*ca.* 200–300 Ω), whereas AWO_4 spectra showed only one charge-transfer resistance, which was a total resistance of FTO and the photocatalyst. The separated FTO resistance was not observed due to the high resistance of scheelite-type compounds, which impedes charge transfer resulting in the collapse of two resistances. By analyzing both coherent data, a distinct behavior of each group of samples can be observed. The obtained results suggest that the presence of tungstates changes the double layer so that it exhibits a more resistive nature than molybdates. Additionally, cyclic voltammograms indicated that AWO_4 compounds are better conductors than the $AMoO_4$ ones. Another possible explanation of improved reversibility for alkali earth metal tungstates suggests a formation of charge carrier channels in the layer of the conductive polymer. Both hypotheses are planned to be studied at a further stage of research.

In order to determine the flat band potential of the obtained samples, a Mott–Schottky analysis was performed (Figure 12). The flat bands (E_{FB}) and capacities (C_{SC}) of these photocatalysts are presented in Figure S5 and Table S1 in the Supporting Information. The positive slope in the linear region of the $f(E) = C_{SC}^{-2}$ (where C_{SC} is the capacitance of the semiconductor) plot was observed. The flat band potential (E_{FB}) was determined from the intersection of the slope with the *X*-axis (*x* position at $y = 0$). The obtained potential was later considered as a conductive band (E_{CB}) of investigated scheelite-type compounds. All the investigated samples are considered n-type semiconductors, which is in agreement with the previous reports.[22,57] Connecting these data with the EIS measurements, a significant difference between alkali earth metal tungstates and molybdates becomes even more visible. $AMoO_4$ compounds exhibited higher values of flat band potential compared to AWO_4. Moreover, the values of C_{SC} and E_{FB} for tungstates were more stable and did not differ very much between samples. On the other hand, the values of molybdates differed depending on the cation present in the compound.

According to Mott–Schottky diagrams and bandgap calculations from DR/UV–vis spectroscopy, the band positions of photocatalysts were calculated (Figure 13). This parameter determines the position of band edges at the

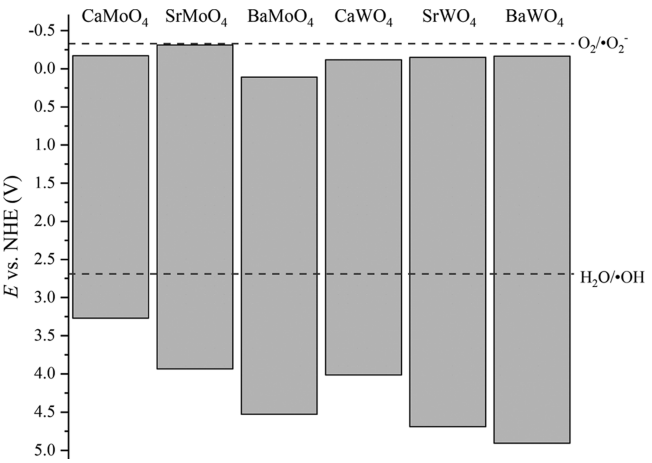

Figure 13. Band edge positions of the obtained photocatalysts determined from the Mott–Schottky analysis and UV–vis absorption. The length of the gray stripes corresponds to the bandgap energy values.

interface between the electrode material and the electrolyte.[58] Therefore, the potential of conduction band electrons and considering the obtained bandgap value, the valence band edge position can be estimated. Based on band positions, it is possible to predict the photocatalytic performance by monitoring the behavior of reactive oxygen species (ROS). The degradation of organic pollutants depends on ROS generation, especially $^{\bullet}OH$ and $^{\bullet}O_2^-$ through water oxidation and reduction of the adsorbed oxygen on the photocatalyst surface.[59] As can be observed in both diagrams, all the semiconductors exhibited a suitable conduction and valence band position to perform the reduction of water. Therefore, there is a possibility of oxidizing phenol using alkali earth metal tungstates and molybdates due to suitable band position to hydroxyl radical generation. It is worth noticing that in the first step of the reaction, the oxidation of phenol by hydroxyl radicals led mainly to the ortho- and para-oriented hydroxy derivatives.[60]

https://doi.org/10.1021/acs.jpcc.1c06481
J. Phys. Chem. C XXXX, XXX, XXX–XXX

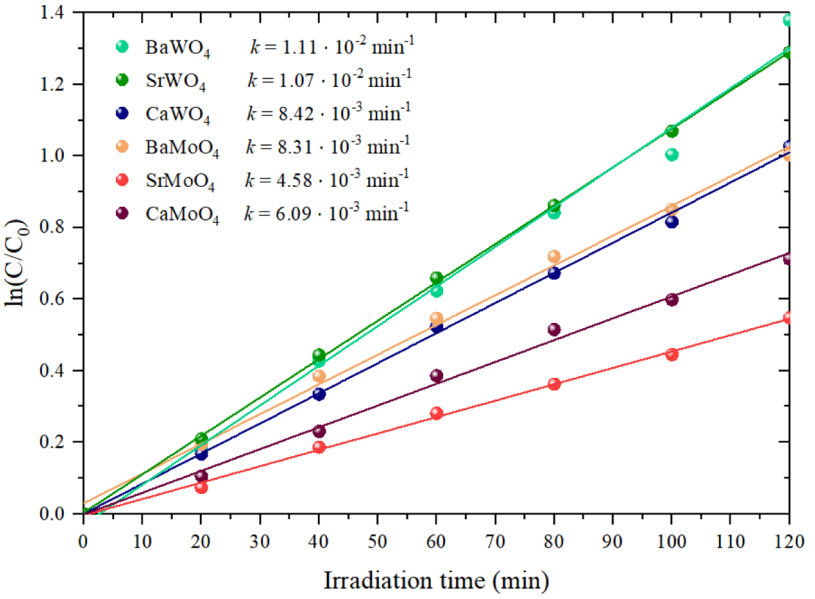

Figure 14. Photocatalytic phenol degradation for different alkali earth scheelite-type compounds.

Table 4. Comparison of ABO_4 with the Reported Unmodified Catalysts for Phenol Degradation

catalyst	initial phenol concentration (mg/L) and catalyst mass (g)	light source	surface area (m^2/g)	rate constant (10^{-3} min^{-1})	surface-area-normalized rate constants[a]	ref.
TiO_2 (Degussa P25)	20 mg/L 0.05 g	300 W Xe lamp, 45 mW/cm^2	55	90	0.033	68
TiO_2 (TBT hydrolysis)	20 mg/L 0.05 g	300 W Xe lamp, 30 mW/cm^2	169	9.8	0.015	69
ZnO	25 mg/L 0.02 g	300 W, light flux not mentioned	no information	5	-	70
WO_3 (Shanghai Chemicals)	40 mg/L 0.12 g[a]	300 W Hg lamp, light flux not mentioned	2.3	0.15	0.0005	71
CeO_2	40 mg/L 0.10 g	Hg lamp 4.4 mW	89	0.80	~0.0001	72
SnO_2	10 mg/L 0.065 g	8 W Hg lamp, 8 mW/cm^2	28	6.20[a]	0.003	73
$CaMoO_4$	20 mg/L 0.05 g	300 W Xe lamp, 45 mW/cm^2	3.88 ± 0.17	6.09 ± 0.20	0.031 ± 0.003	present work
$SrMoO_4$	20 mg/L 0.05 g	300 W Xe lamp, 45 mW/cm^2	4.21 ± 0.04	4.58 ± 0.10	0.022 ± 0.001	present work
$BaMoO_4$	20 mg/L 0.05 g	300 W Xe lamp, 45 mW/cm^2	0.42 ± 0.20	8.31 ± 0.24	0.396 ± 0.201	present work
$CaWO_4$	20 mg/L 0.05 g	300 W Xe lamp, 45 mW/cm^2	10.15 ± 0.29	8.42 ± 0.15	0.017 ± 0.001	present work
$SrWO_4$	20 mg/L 0.05 g	300 W Xe lamp, 45 mW/cm^2	6.98 ± 0.13	10.7 ± 0.09	0.031 ± 0.001	present work
$BaWO_4$	20 mg/L 0.05 g	300 W Xe lamp, 45 mW/cm^2	1.03 ± 0.14	11.1 ± 0.50	0.216 ± 0.040	present work

[a]For better comparison, some parameters were calculated based on the experimental results described in cited reports.

Except for $BaMoO_4$, each photocatalyst has a negative conduction band position. However, the occurrence of a one-electron process of O_2 reduction potential to $^{\bullet}O_2^-$ is doubtful (−0.33 eV for the standard gas state of 1 atm[61]) due to an

https://doi.org/10.1021/acs.jpcc.1c06481
J. Phys. Chem. C XXXX, XXX, XXX−XXX

unsuitable band position. This indicates that the participation of superoxide radicals in the degradation reaction might be limited during the photocatalytic process.[62] However, the redox potential is not constant and is changed with process parameters such as a type of gas or a gas flow. Wardman[63] has calculated the redox potential of $O_2/^{\bullet}O_2^-$ process for 0.2 atm in air and in the case of oxygen concentration equals to 1 M in water. These values were estimated to be −0.29 and −0.16 V, respectively. Therefore, scheelite-type compounds may be capable of generating $^{\bullet}O_2^-$ radicals because the introduction of air and dissolved oxygen in the water system leads to lowering the absolute value of the redox potential. Another possible explanation of these results is that the reduction potential of O_2 might be changed due to the adsorption on the photocatalyst surface. Finally, $^{\bullet}O_2^-$ radicals can also derive from the two-electron process from hydrogen peroxide and further reaction with holes according to eqs 4 and 5

$$O_2 + 2H^+ + 2e \rightarrow H_2O_2 \quad (4)$$

$$H_2O_2 + h^+ \rightarrow^{\bullet} O_2^- + 2H^+ \quad (5)$$

The redox potential of hydrogen peroxide generation is +0.30 eV,[61] so this process can occur in the photocatalytic process with scheelite-type compounds.

3.4. Photocatalytic Activity Analysis. The photocatalytic activity of the as-prepared scheelite-type compounds was evaluated in the reaction of phenol photodegradation. No phenol was degraded in the absence of illumination, indicating no dark reaction at the surface of the obtained samples. Photolysis tests of phenol under UV−vis irradiation without the presence of photocatalyst were also performed. Under the experimental conditions, phenol photolysis was not observed.

The results of phenol degradation in the presence of the obtained materials are presented in Figure 14. The highest photocatalytic activity was observed for $SrWO_4$ and $BaWO_4$ materials. Although their light absorption is limited, scheelite-type compounds exhibited good photocatalytic performance. The comparison of *k*-constant rates with other photocatalysts described in the literature is presented in Table 4. In addition, the surface-area-normalized rate constants were calculated due to better comparison photocatalysts with different specific surface areas.[64] Regarding ABO_4 compounds with a low specific surface area, especially $BaMoO_4$ and $BaWO_4$, the ratio for these materials is similar or higher, even 1 order of magnitude than TiO_2. Therefore, it can be concluded that developing the surface area of tungstates and molybdates may cause more efficient phenol degradation. Remarkably, no information about the photocatalytic performance of alkali earth metal scheelite-type compounds was reported in the literature.

Another observation is the trend to decrease the efficiency while the bandgap value was decreasing. Generally, both photocatalytic and photochemical processes require sufficient energy to generate the electron−holes pairs responsible for the reduction and oxidation processes.[5,65] Therefore, almost all of the reported photocatalysts are semiconductor-based materials with a suitable band structure. It is commonly believed that insulators cannot be used for photocatalytic water treatment due to large bandgaps to be excited by the usual UV and visible light sources.[66,67] However, barium ($BaWO_4$ and $BaMoO_4$) and strontium ($SrWO_4$) compounds possess the highest photocatalytic activity despite the E_g value in the range 4−5 eV.

The light absorption properties and bandgap values are not the main factors influencing the phenol degradation efficiency. In this regard, photoluminescence properties were also studied in detail. While comparing the values of carrier lifetimes with *k*-constants, it can be noted that $SrWO_4$ and $BaWO_4$ revealed the highest $\langle\tau\rangle$ values. By analogy, the short carrier lifetimes contributed to low phenol degradation. It can be assumed that the average lifetime calculated from time-resolved PL decay curves is the main factor that affected the photocatalytic performance. This observation is not entirely consistent with $CaWO_4$, which has a lower $\langle\tau\rangle$ value than $BaMoO_4$, although their phenol photocatalytic degradation is similar. The luminescence decay curve fits the data from a poly-phase exponential decay function with constant parameters τ_1 and τ_2. Meanwhile, the τ_1 value is higher for $CaWO_4$ (129.61 μs) than for $BaMoO_4$ (61.62 μs). The explanation of this discrepancy can be found in thermoluminescence spectra.

$SrWO_4$ and $BaWO_4$ are the most efficient photocatalysts within this scheelite-type series, so this can be explained by no or very low recombination states, which reduce the carrier lifetimes. This observation was described by Wang *et al.*, whose research includes nitrogen-doped anatase titania nanobelts.[74] Although the N 2p levels near the valence band contribute to the visible light absorbance, the band originated from the risen oxygen vacancies. The associated Ti^{3+} species were relatively deep and acted as the recombination centers for the photoinduced electrons and holes, reducing the photocatalytic activity. By analogy, tungstates revealed higher photocatalytic activity than molybdates due to more shallow traps and higher average charge carrier lifetimes. The only exception is probably $CaWO_4$. The photocatalytic activity of $CaWO_4$ can be explained as the presence of trapping centers, which allows for elongating the lifetime carriers. Kato *et al.* have reported that Na-doping in $SrTiO_3$ enhances the activity because new mid-gap states are introduced. The photoexcited electrons were trapped into these states after excitation, so trapped electrons had a longer lifetime than those in undoped $SrTiO_3$.[75] This hypothesis can be confirmed while comparing the τ_1 in this series. This value is the highest from presented scheelite-type compounds, so $CaWO_4$ had a similar photocatalytic performance to $BaMoO_4$. This observation is also in agreement with the TL spectra—two distinct glow peaks were detected for $CaWO_4$, in which the first electron trap causes the prolongation of charge carrier lifetime, whereas the second one is responsible for radiative recombination. However, the second trap was probably a reason for low photocatalytic activity in the AWO_4 series.

3.5. Degradation Mechanism Discussion. During a photocatalytic process, phenol derivatives are formed, indicating the degradation pathway of the organic pollutant. In the case of photoreaction with alkali earth scheelite-type compounds, by HPLC analysis, catechol (CT) and hydroquinone (HQ) were detected as the main intermediate products during the phenol photodegradation reaction. The production of CT and HQ during the reaction is typical for many photocatalysts.[30,68,76] Some works also suggest the formation of benzoquinone (BQ) being in possible equilibrium with hydroquinone.[77,78] However, in this study, BQ presence and the slowdown of the photocatalytic process were not observed. The evolution of phenol removal with the monitored formation of catechol and hydroquinone concentration as a function of photoreaction time using different photocatalysts is presented in Figure S6 in the Supporting Information.

https://doi.org/10.1021/acs.jpcc.1c06481
J. Phys. Chem. C XXXX, XXX, XXX−XXX

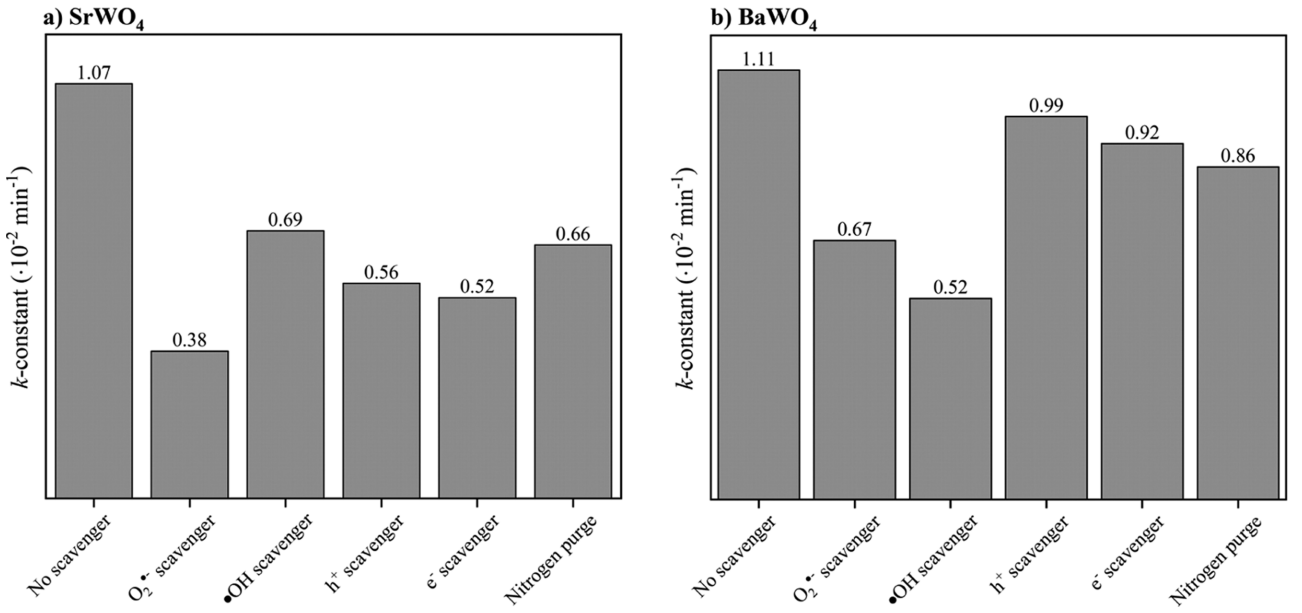

Figure 15. Photocatalytic degradation of phenol in the presence of (a) $SrWO_4$ and (b) $BaWO_4$ and charge carrier scavengers.

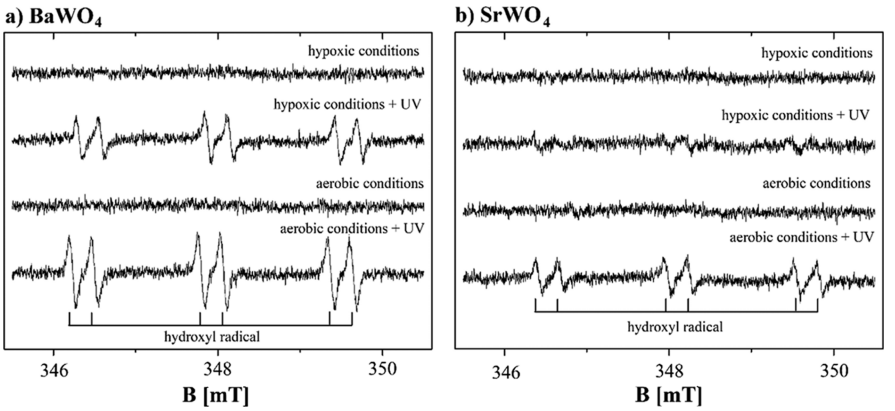

Figure 16. EPR spectra of PBN in (a) $BaWO_4$ and (b) $SrWO_4$ aqueous suspension recorded under hypoxic and aerobic conditions before and after UV irradiation (70 s).

According to the graph, the phenol concentration decreased with the reaction time, whereas the concentration of hydroquinone and catechol increased.

Overall, the photocatalysis mechanism is depicted as the generation of photoexcited electrons and holes in the conduction band and valence band. These charge carriers migrate to the photocatalyst surface and undergo reactions with a water molecule to form reactive oxygen species (ROS). Therefore, the phenol degradation analyses were carried out in the presence of $^{\bullet}O_2^-$, $^{\bullet}OH$, e^-, and h^+ scavengers and under anaerobic conditions (N_2 purging) to understand the phenol degradation pathway. The results of the photocatalytic activity of $BaWO_4$ and $SrWO_4$ in the presence of e^-, h^+, $^{\bullet}O_2^-$, and $^{\bullet}OH$ scavengers, that is, silver nitrate, ammonium oxalate, benzoquinone, and isopropyl alcohol, respectively, and during N_2 purging are presented in Figure 15. $BaWO_4$ and $SrWO_4$ were selected as the most effective photocatalysts in solar-driven phenol degradation.

A significant contribution of both $^{\bullet}OH$ and $^{\bullet}O_2^-$ on the photocatalytic process was observed in both samples. These observations are in agreement with other reports, which confirm that hydroxyl and superoxide radicals are the main factors that contribute to phenol oxidation.[60,76] It suggests that water oxidation, as well as oxygen reduction, can be efficiently performed in the presence of $BaWO_4$ or $SrWO_4$ photocatalysts. Furthermore, in the case of $SrWO_4$, oxygen reduction was predominant in comparison with $BaWO_4$ due to the higher observed effect of $^{\bullet}O2^-$ scavenger as well as an e^- scavenger and N_2 purge to eliminate O_2 from the suspension. On the other hand, $BaWO_4$ seems more suitable for the $^{\bullet}OH$ generation, which agrees with the observed lowering of the valence band potential for this compound. Our overall results suggest that changing the cation in the AWO_4 structure affects the generation ability of ROS generated during irradiation. This effect might be possible due to (i) morphology change of the sample or facet effect in the case of $BaWO_4$ or (ii) modified electronic structure of the conduction band.

$BaWO_4$ and $SrWO_4$ were selected for photochemical EPR measurements. Figure 16 shows the EPR spectra of PBN in $BaWO_4$ (Figure 16a) and $SrWO_4$ (Figure 16b) aqueous suspension. The presented spectra of the suspensions that were not irradiated showed no signals from short-lived $^{\bullet}O_2-$ and $^{\bullet}OH$ radicals trapped on PBN for both hypoxic conditions or aerobic. The spectra of the UV-irradiated suspensions consist

https://doi.org/10.1021/acs.jpcc.1c06481
J. Phys. Chem. C XXXX, XXX, XXX−XXX

of sextets described by spin Hamiltonian parameters (A^N = 1.56 mT, A^H = 0.27 mT, and g = 2.0057),[79−81] which clearly indicate that the PBN traps hydroxyl radicals. It should be noted that the intensity of the EPR spectra recorded under hypoxic conditions was less intense than the spectra obtained under aerobic conditions. The formation of hydroxyl radicals can take place under hypoxic conditions, in opposite to superoxide radicals. On the other hand, the superoxide radical anion can transform directly into a non-paramagnetic form or participate in the formation of the hydroxyl radical. The above statement explains the EPR results in which, due to aerobic conditions, a higher concentration of trapped hydroxyl radicals was observed. Despite the lack of lines in EPR spectra that could be attributed to the $^{\bullet}O_2-$ radical, the decrease in the number of trapped $^{\bullet}OH$ radicals under hypoxic conditions is also an indirect evidence of the superoxide radical creation.

The possible mechanism of the phenol degradation can be described as follows: the $^{\bullet}OH$ radicals initiate the oxidation of phenol molecules, explaining the decline of k-constant for both tungstates. The performed analysis is consistent with HPLC analysis, which indicates the formation of catechol and hydroquinone. These derivatives are the results of phenol oxidation by hydroxyl radicals. After further oxidation of phenol derivatives, superoxide radicals ($^{\bullet}O_2^-$) are needed to break the benzyl ring and mineralize it to CO_2. An increased ability of $SrWO_4$ to reduce oxygen would especially explain the higher TOC removal observed for this sample due to the possible aromatic ring breaking with $^{\bullet}O_2^-$. In the case of $BaWO_4$, the concentration of superoxide radicals is probably too low to open the benzyl ring; therefore, no mineralization was observed[82] (see Figure S7 in the Supporting Information).

3.6. Stability Test. $SrWO_4$ and $SrMoO_4$ compounds with the highest mineralization efficiency measured as a TOC removal were selected to study the stability and reusability of ABO_4 photocatalysts. After each 120 min cycle, photocatalysts were separated and used in another run without any treatment. The obtained results of phenol degradation are presented in Figure S8 in the Supporting Information. No significant loss in photocatalytic activity was noticed after three subsequent cycles of degradation. Moreover, XRD analyses (Figure S9 in the Supporting Information) performed after a single photocatalytic degradation reaction and three subsequent degradation cycles confirmed that scheelite-type compounds are stable after the photocatalytic process and can be reused without specific treatment. Finally, the SEM images of photocatalysts after degradation processes (Figures S10 and S11 in the Supporting Information) indicate that only partial deagglomeration is observed, which is typical for photocatalytic reactions in water systems.

4. CONCLUSIONS

To summarize, a simple synthesis of alkaline earth metal scheelite-type compounds was developed. The photocatalytic activity under simulated solar light irradiation for phenol degradation using AWO_4- and $AMoO_4$-based photocatalysts (A = Ca, Sr, and Ba) was reported for the first time. The morphologies of the potential photocatalyst, together with BET measurements, were described. Despite the microcrystals or microsphere formation and low surface area, all samples exhibit photocatalytic activity toward phenol degradation. Although ABO_4 compounds absorb mainly UV light, the photon amount was sufficient to create photogenerated electron−hole pairs. The thermoluminescence glow curves showed the presence of energy traps, which allow absorbing light at higher wavelengths that it could be suggested by bandgap calculations. Remarkably, the charge carrier lifetime was the crucial factor influencing the photocatalytic performance of the as-synthesized materials. $BaWO_4$ and $SrWO_4$, with the longest $\langle\tau\rangle$ value, demonstrated the highest photodegradation rate constants. Ultimately, AWO_4s are more efficient photocatalysts than $AMoO_4$s because of the possible conduction through charge carrier channels as well as more resistive characteristic, which was observed during electrochemical studies. In addition, molybdates had deeper electron traps than tungstates, which was a reason for their lower photocatalytic activity. Finally, the photocatalytic processes with charge carrier scavengers indicate the significant role of $^{\bullet}OH$ and $^{\bullet}O_2^-$ radicals, which oxidize phenol to hydroquinone and catechol. An increased ability of $SrWO_4$ to reduce oxygen explained the observed phenol mineralization due to the predominant role of $^{\bullet}O_2^-$, e^- and dissolved oxygen in phenol photocatalytic degradation.

The obtained results provide information about the unique physicochemical properties of alkali earth metal scheelite-type compounds and shed new light on the photocatalytic performance of AWO_4 and $AMoO_4$. The precise characteristics facilitate further investigation of these compounds and find novel solutions for enhancing photocatalytic performance in wide-bandgap semiconductors.

■ ASSOCIATED CONTENT

Supporting Information

The Supporting Information is available free of charge at https://pubs.acs.org/doi/10.1021/acs.jpcc.1c06481.

Size distribution of nanoparticles or microcrystals of scheelite-type compounds; adsorption isotherms and pore distributions of scheelite-type compounds; bandgap calculations based on Tauc's method for scheelite-type compounds; excitation spectra of scheelite-type compounds; determination of flat bands and capacity of ABO_4 compounds; phenol, hydroquinone, and catechol concentration *versus* irradiation time during photocatalytic process for all samples; TOC measurements for scheelite-type compounds after 120 min of photocatalytic process; stability tests of scheelite-type compounds (XRD patterns and SEM images), stability tests of $SrWO_4$ and $SrMoO_4$ after three degradation cycles (XRD patterns and SEM images); and efficiency of phenol degradation after 120 min of the photocatalytic process after three degradation cycles (PDF)

■ AUTHOR INFORMATION

Corresponding Authors

Marta Kowalkińska − *Department of Process Engineering and Chemical Technology, Faculty of Chemistry, Gdańsk University of Technology, Gdańsk 80-233, Poland;* orcid.org/0000-0003-0518-7508; Email: marta.kowalkinska@pg.edu.pl

Anna Zielińska-Jurek − *Department of Process Engineering and Chemical Technology, Faculty of Chemistry, Gdańsk University of Technology, Gdańsk 80-233, Poland;* orcid.org/0000-0002-9830-1797; Email: annjurek@pg.edu.pl

https://doi.org/10.1021/acs.jpcc.1c06481
J. Phys. Chem. C XXXX, XXX, XXX−XXX

Authors

Paweł Głuchowski − *Institute of Low Temperature and Structural Research, Polish Academy of Sciences, Wrocław 50-422, Poland;* orcid.org/0000-0003-2566-1422

Tomasz Swebocki − *Department of Analytical Chemistry, Faculty of Chemistry, University of Gdansk, Gdańsk 80-308, Poland; Institute of Interdisciplinary Research (USR 3078), French National Centre for Scientific Research, Villeneuve-d'Ascq F-59652, France*

Tadeusz Ossowski − *Department of Analytical Chemistry, Faculty of Chemistry, University of Gdansk, Gdańsk 80-308, Poland*

Adam Ostrowski − *Institute of Molecular Physics, Polish Academy of Sciences, Poznań 60-179, Poland*

Waldemar Bednarski − *Institute of Molecular Physics, Polish Academy of Sciences, Poznań 60-179, Poland*

Jakub Karczewski − *Institute of Nanotechnology and Materials Engineering, Faculty of Applied Physics and Mathematics, Gdańsk University of Technology, Gdańsk 80-233, Poland*

Complete contact information is available at: https://pubs.acs.org/10.1021/acs.jpcc.1c06481

Notes

The authors declare no competing financial interest.

■ ACKNOWLEDGMENTS

This research was financially supported by the Polish National Science Centre (grant no. NCN 2018/30/E/ST5/00845). We also acknowledge Bogusław Macalik from the Polish Academy of Sciences for reflectance spectra measurements.

■ REFERENCES

(1) Oturan, M. A.; Aaron, J.-J. Advanced Oxidation Processes in Water/Wastewater Treatment: Principles and Applications. A Review. *Crit. Rev. Environ. Sci. Technol.* **2014**, *44*, 2577−2641.

(2) Howe, R. F. Recent Developments in Photocatalysis. *Dev. Chem. Eng. Miner. Process.* **1998**, *6*, 55−84.

(3) Ahmed, S. N.; Haider, W. Heterogeneous Photocatalysis and Its Potential Applications in Water and Wastewater Treatment: A Review. *Nanotechnology* **2018**, *29*, 342001.

(4) Schneider, J.; Matsuoka, M.; Takeuchi, M.; Zhang, J.; Horiuchi, Y.; Anpo, M.; Bahnemann, D. W. Understanding TiO_2 Photocatalysis: Mechanisms and Materials. *Chem. Rev.* **2014**, *114*, 9919−9986.

(5) Fujishima, A.; Zhang, X.; Tryk, D. TiO_2 Photocatalysis and Related Surface Phenomena. *Surf. Sci. Rep.* **2008**, *63*, 515−582.

(6) Li, W.; Ismat Shah, S. Semiconductor Nanoparticles for Photocatalysis. *Encycl. Nanosci. Nanotechnol.* **2004**, *9*, 669−695.

(7) Hsu, L. C.; Galli, P. E. Origin of the Scheelite-Powellite Series of Minerals. *Econ. Geol.* **1973**, *68*, 681−696.

(8) Fan, L.; Fan, Y. X.; Duan, Y. H.; Wang, Q.; Wang, H. T.; Jia, G. H.; Tu, C. Y. Continuous-Wave Intracavity Raman Laser at 1179.5 Nm with $SrWO_4$ Raman Crystal in Diode-End-Pumped Nd:YVO_4 Laser. *Appl. Phys. B: Lasers Opt.* **2009**, *94*, 553−557.

(9) Šulc, J.; Jelínková, H.; Basiev, T. T.; Doroschenko, M. E.; Ivleva, L. I.; Osiko, V. V.; Zverev, P. G. Nd:$SrWO_4$ and Nd:$BaWO_4$ Raman Lasers. *Opt. Mater.* **2007**, *30*, 195−197.

(10) Michail, C.; Valais, I.; Fountos, G.; Bakas, A.; Fountzoula, C.; Kalyvas, N.; Karabotsos, A.; Sianoudis, I.; Kandarakis, I. Luminescence Efficiency of Calcium Tungstate ($CaWO_4$) under X-Ray Radiation: Comparison with Gd_2O_2S:Tb. *Meas.: J. Int. Meas. Confed.* **2018**, *120*, 213−220.

(11) Zhang, X.; Lin, J.; Mikhailik, V. B.; Kraus, H. Studies of Scintillation Properties of $CaMoO_4$ at Millikelvin Temperatures. *Appl. Phys. Lett.* **2015**, *106*, 241904.

(12) Dutta, S.; Som, S.; Sharma, S. K. Luminescence and Photometric Characterization of K+ Compensated $CaMoO_4$:Dy3+ Nanophosphors. *Dalton Trans.* **2013**, *42*, 9654−9661.

(13) Zhang, J.; Wang, Y.; Zhai, Z.; Chen, G. Investigations on Morphology, Photoluminescence and Cathodoluminescence of $SrWO_4$ and $SrWO_4$:Tb^{3+}. *Opt. Mater.* **2014**, *38*, 126−130.

(14) Abreu, M. F. C.; Motta, F. V.; Lima, R. C.; Li, M. S.; Longo, E.; Marques, A. P. D. A. Effect of Process Parameters on Photophysical Properties and Barium Molybdate Phosphors Characteristics. *Ceram. Int.* **2014**, *40*, 6719−6729.

(15) Gou, Y.; Liu, Q.; Shi, X.; Asiri, A. M.; Hu, J.; Sun, X. $CaMoO_4$ Nanosheet Arrays for Efficient and Durable Water Oxidation Electrocatalysis under Alkaline Conditions. *Chem. Commun.* **2018**, *54*, 5066−5069.

(16) Gonçalves, R. F.; Cavalcante, L. S.; Nogueira, I. C.; Longo, E.; Godinho, M. J.; Sczancoski, J. C.; Mastelaro, V. R.; Pinatti, I. M.; Rosa, I. L. V.; Marques, A. P. A. Rietveld Refinement, Cluster Modelling, Growth Mechanism and Photoluminescence Properties of $CaWO_4$:Eu^{3+} Microcrystals. *CrystEngComm* **2015**, *17*, 1654−1666.

(17) Momma, K.; Izumi, F. VESTA 3 for Three-Dimensional Visualization of Crystal, Volumetric and Morphology Data. *J. Appl. Crystallogr.* **2011**, *44*, 1272−1276.

(18) Shivakumara, C.; Saraf, R.; Behera, S.; Dhananjaya, N.; Nagabhushana, H. Scheelite-Type MWO_4 (M = Ca, Sr and Ba) Nanophosphors: Facile Synthesis, Structural Characterization, Photoluminescence and Photocatalytic Properties. *Mater. Res. Bull.* **2015**, *61*, 422−432.

(19) Zhu, Y.; Zheng, G.; Dai, Z.; Zhang, L.; Ma, Y. Photocatalytic and Luminescent Properties of $SrMoO_4$ Phosphors Prepared via Hydrothermal Method with Different Stirring Speeds. *J. Mater. Sci. Technol.* **2017**, *33*, 23−29.

(20) Ghoreishi, S. M. Facile Synthesis and Characterization of $CaWO_4$ Nanoparticles Using a New Schiff Base as Capping Agent: Enhanced Photocatalytic Degradation of Methyl Orange. *J. Mater. Sci. Mater. Electron.* **2017**, *28*, 14833−14838.

(21) Bi, J.; Wu, L.; Zhang, Y.; Li, Z.; Li, J.; Fu, X. Solvothermal Preparation, Electronic Structure and Photocatalytic Properties of PbMoO4 and $SrMoO_4$. *Appl. Catal., B* **2009**, *91*, 135−143.

(22) Huerta-Flores, A. M.; Juárez-Ramírez, I.; Torres-Martínez, L. M.; Carrera-Crespo, J. E.; Gómez-Bustamante, T.; Sarabia-Ramos, O. Synthesis of $AMoO_4$ (A = Ca, Sr, Ba) Photocatalysts and Their Potential Application for Hydrogen Evolution and the Degradation of Tetracycline in Water. *J. Photochem. Photobiol., A* **2018**, *356*, 29−37.

(23) Luttrell, T.; Halpegamage, S.; Tao, J.; Kramer, A.; Sutter, E.; Batzill, M. Why Is Anatase a Better Photocatalyst than Rutile? - Model Studies on Epitaxial TiO_2 Films. *Sci. Rep.* **2015**, *4*, 4043.

(24) Dong, F.; Xiong, T.; Sun, Y.; Lu, L.; Zhang, Y.; Zhang, H.; Huang, H.; Zhou, Y.; Wu, Z. Exploring the Photocatalysis Mechanism on Insulators. *Appl. Catal., B* **2017**, *219*, 450−458.

(25) Cui, W.; Chen, L.; Li, J.; Zhou, Y.; Sun, Y.; Jiang, G.; Lee, S. C.; Dong, F. Ba-Vacancy Induces Semiconductor-like Photocatalysis on Insulator $BaSO_4$. *Appl. Catal., B* **2019**, *253*, 293−299.

(26) Li, K.; Zhang, S.; Tan, Q.; Wu, X.; Li, Y.; Li, Q.; Fan, J.; Lv, K. Insulator in Photocatalysis: Essential Roles and Activation Strategies. *Chem. Eng. J.* **2021**, *426*, 130772.

(27) Adán, C.; Bahamonde, A.; Fernández-García, M.; Martínez-Arias, A. Structure and Activity of Nanosized Iron-Doped Anatase TiO_2 Catalysts for Phenol Photocatalytic Degradation. *Appl. Catal., B* **2007**, *72*, 11−17.

(28) Dang, T. T. T.; Le, S. T. T.; Channei, D.; Khanitchaidecha, W.; Nakaruk, A. Photodegradation Mechanisms of Phenol in the Photocatalytic Process. *Res. Chem. Intermed.* **2016**, *42*, 5961−5974.

(29) Krivec, M.; Pohar, A.; Likozar, B.; Dražić, G. Hydrodynamics, Mass Transfer, and Photocatalytic Phenol Selective Oxidation Reaction Kinetics in a Fixed TiO_2 Microreactor. *AIChE J.* **2015**, *61*, 572−581.

(30) Sobczyński, A.; Duczmal, Ł.; Zmudziński, W. Phenol Destruction by Photocatalysis on TiO_2: An Attempt to Solve the Reaction Mechanism. *J. Mol. Catal. A: Chem.* **2004**, *213*, 225−230.

https://doi.org/10.1021/acs.jpcc.1c06481
J. Phys. Chem. C XXXX, XXX, XXX−XXX

(31) Aslam, M.; Ismail, I. M. I.; Chandrasekaran, S.; Hameed, A. Morphology Controlled Bulk Synthesis of Disc-Shaped WO_3 Powder and Evaluation of Its Photocatalytic Activity for the Degradation of Phenols. *J. Hazard. Mater.* **2014**, *276*, 120−128.
(32) Soltanali, S.; Darian, J. T. Synthesis of Mesoporous SAPO-34 Catalysts in the Presence of MWCNT, CNF, and GO as Hard Templates in MTO Process. *Powder Technol.* **2019**, *355*, 127−134.
(33) Tauc, J. Optical Properties and Electronic Structure of Amorphous Ge and Si. *Mater. Res. Bull.* **1968**, *3*, 37−46.
(34) Bailiff, I. K. Characteristics of Time-Resolved Luminescence in Quartz. *Radiat. Meas.* **2000**, *32*, 401−405.
(35) Jones, M.; Nedeljkovic, J.; Ellingson, R. J.; Nozik, A. J.; Rumbles, G. Photoenhancement of Luminescence in Colloidal CdSe Quantum Dot Solutions. *J. Phys. Chem. B* **2003**, *107*, 11346−11352.
(36) Wang, Y.; Xu, K.; Li, D.; Zhao, H.; Hu, Z. Persistent Luminescence and Photocatalytic Properties of Ga_2O_3:Cr^{3+},Zn^{2+} Phosphors. *Opt. Mater.* **2014**, *36*, 1798−1801.
(37) Cooke, D. W.; Bennett, B. L.; Farnum, E. H.; Hults, W. L.; Muenchausen, R. E.; Smith, J. L. Thermally Stimulated Luminescence from X-Irradiated Porous Silicon. *Appl. Phys. Lett.* **1997**, *70*, 3594−3596.
(38) Winer, A. M.; Breuer, G. M.; Carter, W. P. L.; Darnall, K. R.; Pitts, J. N. Effects of Ultraviolet Spectral Distribution on the Photochemistry of Simulated Polluted Atmospheres. *Atmos. Environ.* **1979**, *13*, 989−998.
(39) Cavalcante, L. S.; Sczancoski, J. C.; Tranquilin, R. L.; Varela, J. A.; Longo, E.; Orlandi, M. O. Growth Mechanism of Octahedron-like $BaMoO_4$ Microcrystals Processed in Microwave-Hydrothermal: Experimental Observations and Computational Modeling. *Particuology* **2009**, *7*, 353−362.
(40) Oliveira, M. C.; Gracia, L.; Nogueira, I. C.; do Carmo Gurgel, M. F.; Mercury, J. M. R.; Longo, E.; Andrés, J. Synthesis and Morphological Transformation of $BaWO_4$ Crystals: Experimental and Theoretical Insights. *Ceram. Int.* **2016**, *42*, 10913−10921.
(41) Alencar, L. D. S.; Mesquita, A.; Feitosa, C. A. C.; Balzer, R.; Probst, L. F. D.; Batalha, D. C.; Rosmaninho, M. G.; Fajardo, H. V.; Bernardi, M. I. B. Preparation, Characterization and Catalytic Application of Barium Molybdate ($BaMoO_4$) and Barium Tungstate (BaWO4) in the Gas-Phase Oxidation of Toluene. *Ceram. Int.* **2017**, *43*, 4462−4469.
(42) Iervolino, G.; Zammit, I.; Vaiano, V.; Rizzo, L. Limitations and Prospects for Wastewater Treatment by UV and Visible-Light-Active Heterogeneous Photocatalysis: A Critical Review. *Top. Curr. Chem.* **2020**, *378*, 7.
(43) Loeb, S. K.; Alvarez, P. J. J.; Brame, J. A.; Cates, E. L.; Choi, W.; Crittenden, J.; Dionysiou, D. D.; Li, Q.; Li-Puma, G.; Quan, X.; et al. The Technology Horizon for Photocatalytic Water Treatment: Sunrise or Sunset? *Environ. Sci. Technol.* **2019**, *53*, 2937−2947.
(44) Jędrzejczyk, M.; Zbudniewek, K.; Rynkowski, J.; Keller, V.; Grams, J.; Ruppert, A. M.; Keller, N. Wide Band Gap Ga_2O_3 as Efficient UV-C Photocatalyst for Gas-Phase Degradation Applications. *Environ. Sci. Pollut. Res.* **2017**, *24*, 26792−26805.
(45) Zhang, Y.; Holzwarth, N. A. W.; Williams, R. T. Electronic band structures of the scheelite materialsCaMoO4, $CaWO_4$, $PbMoO_4$ and $PbWO_4$. *Phys. Rev. B: Condens. Matter Mater. Phys.* **1998**, *57*, 12738−12750.
(46) Singh, A.; Dutta, D. P.; Ramkumar, J.; Bhattacharya, K.; Tyagi, A. K.; Fulekar, M. H. Serendipitous Discovery of Super Adsorbent Properties of Sonochemically Synthesized Nano BaWO4. *RSC Adv.* **2013**, *3*, 22580−22590.
(47) Thongtem, T.; Kungwankunakorn, S.; Kuntalue, B.; Phuruangrat, A.; Thongtem, S. Luminescence and Absorbance of Highly Crystalline $CaMoO_4$, $SrMoO_4$, $CaWO_4$ and $SrWO_4$ Nanoparticles Synthesized by Co-Precipitation Method at Room Temperature. *J. Alloys Compd.* **2010**, *506*, 475−481.
(48) Li Puma, G.; Yue, P. L. Effect of the Radiation Wavelength on the Rate of Photocatalytic Oxidation of Organic Pollutants. *Ind. Eng. Chem. Res.* **2002**, *41*, 5594−5600.
(49) Jing, L.; Xin, B.; Yuan, F.; Xue, L.; Wang, B.; Fu, H. Effects of Surface Oxygen Vacancies on Photophysical and Photochemical Processes of Zn-Doped TiO_2 Nanoparticles and Their Relationships. *J. Phys. Chem. B* **2006**, *110*, 17860−17865.
(50) Liqiang, J.; Yichun, Q.; Baiqi, W.; Shudan, L.; Baojiang, J.; Libin, Y.; Wei, F.; Honggang, F.; Jiazhong, S. Review of Photoluminescence Performance of Nano-Sized Semiconductor Materials and Its Relationships with Photocatalytic Activity. *Sol. Energy Mater. Sol. Cells* **2006**, *90*, 1773−1787.
(51) Liqiang, J.; Xiaojun, S.; Baifu, X.; Baiqi, W.; Weimin, C.; Honggang, F. The Preparation and Characterization of La Doped TiO_2 Nanoparticles and Their Photocatalytic Activity. *J. Solid State Chem.* **2004**, *177*, 3375−3382.
(52) Fujihara, K.; Izumi, S.; Ohno, T.; Matsumura, M. Time-Resolved Photoluminescence of Particulate TiO_2 Photocatalysts Suspended in Aqueous Solutions. *J. Photochem. Photobiol., A* **2000**, *132*, 99−104.
(53) Rajashekharaiah, A. S.; Vidya, Y. S.; Anantharaju, K. S.; Darshan, G. P.; Lalitha, P.; Sharma, S. C.; Nagabhushana, H. Photoluminescence, Thermoluminescence and Photocatalytic Studies of Sonochemical Synthesis of $Bi_2Zr_2O_7$:Sm^{3+} Nanomaterials. *J. Mater. Sci. Mater. Electron.* **2020**, *31*, 15627−15643.
(54) Kong, M.; Li, Y.; Chen, X.; Tian, T.; Fang, P.; Zheng, F.; Zhao, X. Tuning the Relative Concentration Ratio of Bulk Defects to Surface Defects in TiO_2 Nanocrystals Leads to High Photocatalytic Efficiency. *J. Am. Chem. Soc.* **2011**, *133*, 16414−16417.
(55) Kohtani, S.; Kamoi, Y.; Yoshioka, E.; Miyabe, H. Kinetic Study on Photocatalytic Hydrogenation of Acetophenone Derivatives on Titanium Dioxide. *Catal. Sci. Technol.* **2014**, *4*, 1084−1091.
(56) Cirocka, A.; Zarzeczańska, D.; Wcisło, A.; Ryl, J.; Bogdanowicz, R.; Finke, B.; Ossowski, T. Tuning of the Electrochemical Properties of Transparent Fluorine-Doped Tin Oxide Electrodes by Microwave Pulsed-Plasma Polymerized Allylamine. *Electrochim. Acta* **2019**, *313*, 432−440.
(57) Luo, J.; Bai, X.; Li, Q.; Yu, X.; Li, C.; Wang, Z.; Wu, W.; Liang, Y.; Zhao, Z.; Liu, H. Band Structure Engineering of Bioinspired Fe Doped $SrMoO_4$ for Enhanced Photocatalytic Nitrogen Reduction Performance. *Nano Energy* **2019**, *66*, 104187.
(58) Luévano-Hipólito, E.; Torres-Martínez, L. M. Ink-Jet Printing Films of Molybdates of Alkaline Earth Metals with Scheelite Structure Applied in the Photocatalytic CO_2 Reduction. *J. Photochem. Photobiol., A* **2019**, *368*, 15−22.
(59) Augugliaro, V.; Bellardita, M.; Loddo, V.; Palmisano, G.; Palmisano, L.; Yurdakal, S. Overview on Oxidation Mechanisms of Organic Compounds by TiO_2 in Heterogeneous Photocatalysis. *J. Photochem. Photobiol., C* **2012**, *13*, 224−245.
(60) Lv, K.; Guo, X.; Wu, X.; Li, Q.; Ho, W.; Li, M.; Ye, H.; Du, D. Photocatalytic Selective Oxidation of Phenol to Produce Dihydroxybenzenes in a TiO_2/UV System: Hydroxyl Radical versus Hole. *Appl. Catal., B* **2016**, *199*, 405−411.
(61) Nosaka, Y.; Nosaka, A. Y. Generation and Detection of Reactive Oxygen Species in Photocatalysis. *Chem. Rev.* **2017**, *117*, 11302−11336.
(62) Augugliaro, V.; Palmisano, L.; Sclafani, A.; Minero, C.; Pelizzetti, E. Photocatalytic Degradation of Phenol in Aqueous Titanium Dioxide Dispersions. *Toxicol. Environ. Chem.* **1988**, *16*, 89−109.
(63) Wardman, P. Reduction Potentials of One Electron Couples Involving Free Radicals in Aqueous Solution. *J. Phys. Chem. Ref. Data* **1989**, *18*, 1637−1755.
(64) Zhong, J.; Zhao, Y.; Ding, L.; Ji, H.; Ma, W.; Chen, C.; Zhao, J. Opposite Photocatalytic Oxidation Behaviors of BiOCl and TiO_2: Direct Hole Transfer vs. Indirect OH Oxidation. *Appl. Catal., B* **2019**, *241*, 514−520.
(65) Chen, X.; Shen, S.; Guo, L.; Mao, S. S. Semiconductor-Based Photocatalytic Hydrogen Generation. *Chem. Rev.* **2010**, *110*, 6503−6570.

https://doi.org/10.1021/acs.jpcc.1c06481
J. Phys. Chem. C XXXX, XXX, XXX−XXX

(66) Li, R.; Wang, X.; Jin, S.; Zhou, X.; Feng, Z.; Li, Z.; Shi, J.; Zhang, Q.; Li, C. Photo-Induced H_2 Production from a CH_3OH-H_2O Solution at Insulator Surface. *Sci. Rep.* **2015**, *5*, 13475.
(67) Yu, Z.; Chen, X.-Q.; Kang, X.; Xie, Y.; Zhu, H.; Wang, S.; Ullah, S.; Ma, H.; Wang, L.; Liu, G.; et al. Noninvasively Modifying Band Structures of Wide-Bandgap Metal Oxides to Boost Photocatalytic Activity. *Adv. Mater.* **2018**, *30*, No. e1706259.
(68) Dudziak, S.; Kowalkińska, M.; Karczewski, J.; Pisarek, M.; Siuzdak, K.; Kubiak, A.; Siwińska-Ciesielczyk, K.; Zielińska-Jurek, A. Solvothermal Growth of {0 0 1} Exposed Anatase Nanosheets and Their Ability to Mineralize Organic Pollutants. The Effect of Alcohol Type and Content on the Nucleation and Growth of TiO_2 Nanostructures. *Appl. Surf. Sci.* **2021**, *563*, 150360.
(69) Bielan, Z.; Dudziak, S.; Sulowska, A.; Pelczarski, D.; Ryl, J.; Zielińska-Jurek, A. Preparation and Characterization of Defective TiO_2. The Effect of the Reaction Environment on Titanium Vacancies Formation. *Materials* **2020**, *13*, 2763.
(70) Jiang, J.; Wang, H.; Chen, X.; Li, S.; Xie, T.; Wang, D.; Lin, Y. Enhanced Photocatalytic Degradation of Phenol and Photogenerated Charges Transfer Property over BiOI-Loaded ZnO Composites. *J. Colloid Interface Sci.* **2017**, *494*, 130−138.
(71) Wan, L.; Sheng, J.; Chen, H.; Xu, Y. Different Recycle Behavior of Cu^{2+} and Fe^{3+} Ions for Phenol Photodegradation over TiO_2 and WO_3. *J. Hazard. Mater.* **2013**, *262*, 114−120.
(72) Castañeda, C.; Gutiérrez, K.; Alvarado, I.; Martínez, J. J.; Rojas, H.; Tzompantzi, F.; Gómez, R. Effective Phosphated CeO_2 Materials in the Photocatalytic Degradation of Phenol under UV Irradiation. *J. Chem. Technol. Biotechnol.* **2020**, *95*, 3213−3220.
(73) Al-Hamdi, A. M.; Sillanpää, M.; Bora, T.; Dutta, J. Efficient Photocatalytic Degradation of Phenol in Aqueous Solution by SnO_2 :Sb Nanoparticles. *Appl. Surf. Sci.* **2016**, *370*, 229−236.
(74) Wang, J.; Tafen, D. N.; Lewis, J. P.; Hong, Z.; Manivannan, A.; Zhi, M.; Li, M.; Wu, N. Origin of Photocatalytic Activity of Nitrogen-Doped TiO_2 Nanobelts. *J. Am. Chem. Soc.* **2009**, *131*, 12290−12297.
(75) Kato, K.; Jiang, J.; Sakata, Y.; Yamakata, A. Effect of Na-Doping on Electron Decay Kinetics in $SrTiO_3$ Photocatalyst. *ChemCatChem* **2019**, *11*, 6349−6354.
(76) Wysocka, I.; Kowalska, E.; Trzciński, K.; Łapiński, M.; Nowaczyk, G.; Zielińska-Jurek, A. UV-Vis-Induced Degradation of Phenol over Magnetic Photocatalysts Modified with Pt, Pd, Cu and Au Nanoparticles. *Nanomaterials* **2018**, *8*, 28.
(77) Devi, L. G.; Rajashekhar, K. E. A kinetic model based on non-linear regression analysis is proposed for the degradation of phenol under UV/solar light using nitrogen doped TiO_2. *J. Mol. Catal. A: Chem.* **2011**, *334*, 65−76.
(78) Murcia, J. J.; Hidalgo, M. C.; Navío, J. A.; Araña, J.; Doña-Rodríguez, J. M. Study of the Phenol Photocatalytic Degradation over TiO2 Modified by Sulfation, Fluorination, and Platinum Nanoparticles Photodeposition. *Appl. Catal., B* **2015**, *179*, 305−312.
(79) Tero-Kubota, S.; Ikegami, Y.; Kurokawa, T.; Sasaki, R.; Sugioka, K.; Nakano, M. Generation of Free Radicals and Initiation of Radical Reactions in Nitrones−Fe^{2+}−Phosphate Buffer Systems. *Biochem. Biophys. Res. Commun* **1982**, *108*, 1025−1031.
(80) Dodd, N. J. F.; Jha, A. N. Photoexcitation of Aqueous Suspensions of Titanium Dioxide Nanoparticles: An Electron Spin Resonance Spin Trapping Study of Potentially Oxidative Reactions. *Photochem. Photobiol.* **2011**, *87*, 632−640.
(81) Janzen, E.; Kotake, Y.; Randalld, H. Stabilities of Hydroxyl Radical Spin Adducts of PBN-Type Spin Traps. *Free Radic. Biol. Med.* **1992**, *12*, 169−173.
(82) Kowalkińska, M.; Dudziak, S.; Karczewski, J.; Ryl, J.; Trykowski, G.; Zielińska-Jurek, A. Facet Effect of TiO_2 Nanostructures from $TiOF_2$ and Their Photocatalytic Activity. *Chem. Eng. J.* **2021**, *404*, 126493.

https://doi.org/10.1021/acs.jpcc.1c06481
J. Phys. Chem. C XXXX, XXX, XXX−XXX